Zero-Power Tip-Tilt Control of Magnetically Levitated Platforms by

Lateral Displacement of Permanent Magnets

By

James Lin

Student ID Number: 1208001

A Dissertation Submitted to the

Department of Engineering, Graduate School of Engineering

Kochi University of Technology

Kochi, Japan

Supervisor: Dr. Koichi Oka

Co-Supervisor: Dr. Akinori Harada

Committee Members:
Associate Prof. Kyoko Shibata
Dr. Motomichi Sonobe
Dr. Hirokazu Kobayashi

Abstract

Zero-Power Tip-Tilt Control of Magnetically Levitated Platforms by Lateral Displacement of
Permanent Magnets

In this research, control methodologies are developed which allow magnetically levitated platforms to operate with zero-power control under eccentric loading with active tip-tilt control. To the extent of background research conducted, at the time of publication, no other systems exist which have demonstrated zero-power levitation under eccentric loading with active tip-tilt control.

A general approach to zero-power tip-tilt control is mathematically described to allow the control methodology developed to be applied to various systems. Further, two specific hardware configurations are developed, produced, and tested to validate the proposed control strategy. A mathematical formulation is created for both systems and data collected from successful experimental trials from both systems is provided. For one of the configurations, linearized simulations are conducted whose results agree with the experimental data. The hardware used for experimental trials is described in detail.

The first system configuration presented is designed with the goal of investigating the minimum requirements to achieve zero-power tip-tilt control. As such, it employs the minimum required number of 3 hybrid-electromagnets to control the levitated platform in three degrees of freedom. Further, a basic local control strategy is employed.

The second system configuration is designed with the goal of improving system performance and consists of a geometry more suitable for industrial applications. In this configuration, 4 hybrid-electromagnets are employed to control the same 3 degrees-of-freedom with the use of a state-space controller.

Finally, both configurations are compared and the benefits and limitations of each configuration is discussed.

List of Figures

List of Tables

Table of Contents

Chapter 1 – Introduction

1. Definition of Terms

In this section, the technical terms which are included in the title, "Zero-Power Tip-Tilt Control of Magnetically Levitated Platforms by Lateral Displacement of Permanent magnets," are defined.

1a. Zero-Power

With regards to magnetic levitation, zero-power control is a term used to describe a control paradigm where the levitated platform is held by active feedback control in an unstable equilibrium position [1-4]. It is understood by basic principles that a system which is in equilibrium will stay in equilibrium without the need of external interference or power if not perturbed.

Consider the case depicted in Fig 1 where a hybrid-electromagnet (HEM) is suspended under a passive magnetic target. If the air-gap between the HEM and the target is at a certain value, the passive magnetic force and the gravitational force will be exactly equal and no active current will be required through the electromagnetic coil to achieve static equilibrium. However, this is an unstable equilibrium and the HEM will raise or fall if the air-gap is increased or decreased even slightly. Here then, zero-power control aims to control the current through an electromagnetic coil such that the system maintains the equilibrium air-gap.
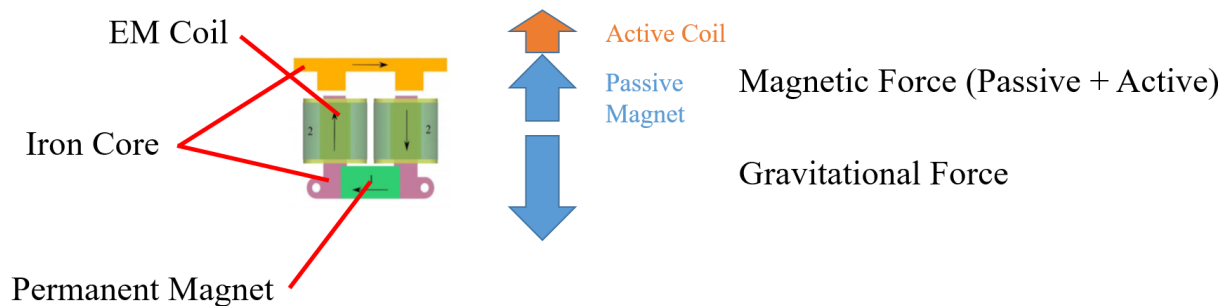
Fig. 1 – Depiction of a HEM suspended under a magnetically permeable target.

In magnetic levitation systems of more than 1 degree-of-freedom (DoF), zero-power control describes a system which allows the platform to be levitated where the current draw of all electromagnetic coils in the system approaches zero. The details of zero-power levitation in more than 1 DoF will be described in greater detail in Chapter 1 Section 2: Basic Principle.

1b. Tip-Tilt Control

Tip-tilt control simplify refers to the ability of a system to actively track an arbitrary pitch and yaw. In magnetic levitation systems of more than 1 DoF, the zero-power tip-tilt of the levitated platform is directly linked to the loading condition of the system. Therefore, with typical levitation systems, zero-power tip-tilt control cannot be achieved under arbitrary eccentric loading [5-6]. The relationship between tip-tilt and zero-power is described in greater detail in Chapter 1 Section 2: Basic Principle.

1c. Lateral Displacement

Lateral displacement of permanent magnets is defined as the displacement of permanent magnets in a direction orthogonal to their attractive magnetic force. When the displacement of permanent magnetics is laterally constrained, no active holding force is required to hold the magnets in place when the levitated system is horizontal.

2. Basic Principle

It is known that the air-gap between an HEM and a magnetic target can be adjusted by controlling the current through the electromagnetic coil [7-8], however, for systems of more than a single DoF, it is not trivial to achieve both zero-power and tip-tilt control simultaneously. This complexity is outlined in Fig. 2.
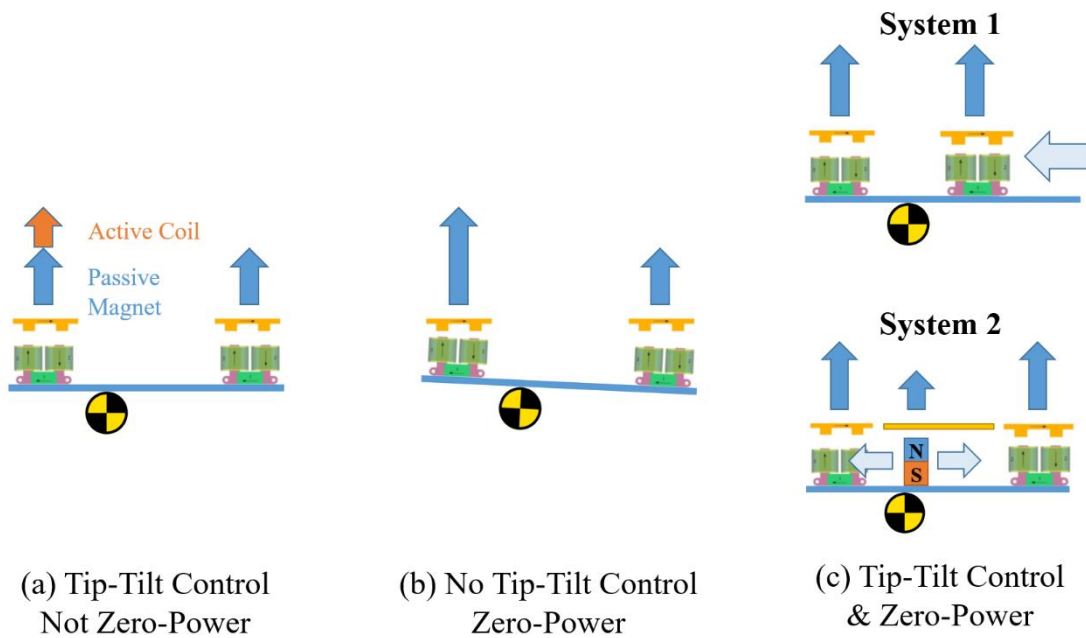
Fig. 2 – (a) A system which is tip-tilt controlled, but not zero power. (b) A system which is zero-power, but not tilt-tilt controlled. (c) The two systems presented in this research which are both tip-tilt controlled and zero-power.

In Fig. 2(a), a tip-tilt controlled levitation system is depicted which uses an active current to account for eccentric loading; this system is tip-tilt controlled, but not zero-power. In Fig. 2(b), instead of using an active current to account for eccentricity, the levitation system decreases the air-gap at one HEM to increase the passive attractive magnetic force; this system is zero-power but not tip-tilt controlled. These two systems are representative of past research on zero-power magnetic levitation [5,9,10].

In this research, the strategy depicted in Fig. 2(c) is proposed where permanent magnets are laterally displaced to account for eccentric loads, allowing the levitation systems to be both zero-power and tip-tilt controlled simultaneously [11-12]. In system 1, the laterally displaced permanent magnets are integrated in the HEMs, while in system 2, the laterally displaced permanent magnets exists independent of the HEMs.

3. System Summary

Table 1 – System Comparison

	System 1	System 2
Number of HEMs	3 (Minimum Requirement)	4 (Input Redundant)
Control Method	Local Control	State-Space Control
Degrees of Freedom	3	3
Permanent Magnet Configuration	Integrated into HEMs	Separate from HEMs
Geometry	Circular	Rectangular

The primary differences between the two systems presented in this research are described in Table 1. Each system will later be described in detail in its own chapter.

In summary, system 1 was designed with the objective of determining the minimum requirements for zero-power tip-tilt control to be achieved. As such, the system is configured with the minimum required 3 HEMs and a basic local controller is employed. A circular geometry was selected for system 1 for manufacturing simplicity.

System 2 was designed with the objective of improving system performance. As such, the system is input redundant with 4 HEMs used to control the same 3 DoFs. Further, a relatively more complicated state-space control strategy is employed. The performance improvement in system 2 is later observed in experimental trails.

4. Assumptions

In the mathematic formulations, it is assumed that all permanent magnets and electromagnetic coils have characteristics that are identical to one another. Further, small angle approximations are used when considering the angular tip-tilt of the system. Where relevant, the validity of these assumptions is addressed.

Chapter 2 – General Theory

This section covers topics of general theory which are used in developing both system 1 and system 2. Of most importance is theory regarding moment balance, as this is the foundation for achieving zero-power tip-tilt control. Zero-power air-gap feedback control is also explained, however, this topic is already the topic of past research [1,3,7].

1. Force Moment Decomposition

An eccentric load on a system can be decomposed into an equivalent force and moment about the center of mass (CoM) of the system. In such a decomposition, it can be interpreted that a force couple is required to counteract the moment about the CoM and an average force is required to counteract the weight of the load. From the perspective of control, force couples can be directly related to current differentials and weight can be directly related to mean current. In general, the decomposition can be described with the linear transformation

$$\begin{Bmatrix} F \\ M_x \\ M_y \end{Bmatrix} = k_i T_{3,n} \begin{Bmatrix} i_1 \\ i_2 \\ i_n \end{Bmatrix}_{n,1} \tag{1}$$

where, k_i is a linearized current-force constant and $T_{3,n}$ is a transformation which is dependent on the location of the n electromagnetic coils. $T_{3,n}$ is defined for the geometric configurations of system 1 and system 1 in their respective chapters.

By decomposing eccentric loads into equivalent force-moments, separate control strategies can be employed to counteract forces and moments independently. The general approach counteracting moments and forces is described in the following sections.

2. Moment Balance by Displacement Control

Moment balance is achieved by the lateral displacement of permanent magnets. The controller which determines the location of the permanent magnets is referred to in this research as the displacement controller. It is the objective of the displacement controller to laterally displace permanent magnets in such a manner that the moment caused by the permanent magnets is equal and opposite to the moment caused by the active currents through the electromagnetic coils

$$\begin{Bmatrix} M_x \\ M_y \end{Bmatrix}_{Displacement} = -\begin{Bmatrix} M_x \\ M_y \end{Bmatrix}_{Currents}. \tag{2}$$

The moment caused by active currents can be described as

$$\begin{Bmatrix} M_x \\ M_y \end{Bmatrix}_{Currents} = k_i T_{2,n} \begin{Bmatrix} i_1 \\ i_2 \\ i_n \end{Bmatrix}_{n,1} \tag{3}$$

where $T_{2,n}$ is a reduced matrix consisting of the second and third rows of $T_{3,n}$. And, the moment caused by the displacement of permanent magnets when the platform is horizontal can be described as

$$\begin{Bmatrix} M_x \\ M_y \end{Bmatrix}_{Displacement} = \begin{bmatrix} 0 & \frac{1}{k_z} \\ -\frac{1}{k_z} & 0 \end{bmatrix} \begin{Bmatrix} C_x \\ C_y \end{Bmatrix}, \tag{4}$$

where C_x and C_y are the coordinates of the centroid of the permanent magnets and k_z is a linearized air-gap-force constant. The complete relationship between permanent magnet centroid and active current can then be given as

$$\begin{Bmatrix} C_x \\ C_y \end{Bmatrix} = -k_i \begin{bmatrix} 0 & k_z \\ -k_z & 0 \end{bmatrix} T_{2,n} \begin{Bmatrix} i_1 \\ i_2 \\ i_n \end{Bmatrix}_{n,1} = Q \begin{Bmatrix} i_1 \\ i_2 \\ i_n \end{Bmatrix}_{n,1} \tag{5}$$

where Q is defined as the equivalent transformation between current and centroid.

The relationship described in (5) is the basic principle used to employ current feedback for the displacement controller. Of greatest importance is the transformation Q which is described for each system in their respective chapters. The exact formulation for the displacement controller for each system is also described in greater detail in their respective chapters.

3. Force Balance by Air-gap Control

Force balance by air-gap control can most easily be understood in a single DoF as was depicted in Fig. 1. Systems of more than a single DoF can be simplified into a single DoF if the average air-gap of all magnets and the average current of all coils is considered. The dynamics of the single DoF problem when linearized about the equilibrium air-gap is described as

$$\ddot{z}_{gap} = \frac{1}{m} \left(k_z z_{gap} + n k_i \bar{\imath} \right). \tag{6}$$

6

where *m* is the mass of the system and *n* is the number of HEMs. This relationship can be seen to be a second order system where the average current is the control input. This is the basic principle which is used for the air-gap controller, where the characteristics of the single DoF problem are already well known from previous research [1,3,7]. The exact implementation of the air-gap controller is described for each system in its respective chapter.

1. PID Control

Positional-integral-differential controllers are used in this research for the air-gap controllers for both systems 1 and 2. The mathematical form of the PID controllers used is given as

$$PID(z) = K_P + K_I T_s \frac{1}{z-1} + K_D \frac{N}{1+NT_s\frac{1}{z-1}}, \tag{7}$$

where K_P, K_I, K_D, N, and T_s are the proportional gain, integral gain, derivative gain, filtering coefficient, and sampling time respectively. In the case where PD control is employed, the same general form is used where it is understood the integral gain is zero. The input for each PID controller is the error between a target state and the actual state of the system. How the target is determined for each system will be described in its respective chapter.

1. Definition of 'Activation' and 'Deactivation'

In this research, when portions of a control system are described as being 'activated' and 'deactivated' this corresponds mathematically to two conditions. For a system to be considered deactivated, the output of that system must be an array of zeros of appropriate size for the output. When a system is activated, the state of any integrators in the system is reset and the starting state is an array of zeros of the appropriate size for the output.

Chapter 3 – System 1

1. Mathematical Formulation
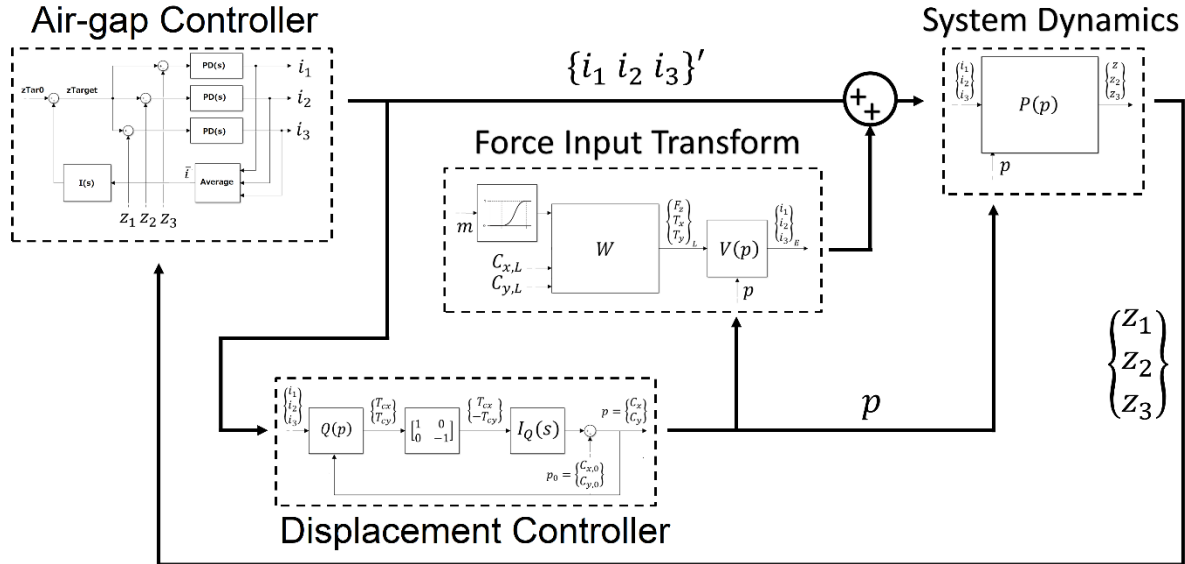
Fig. 3 –A block diagram of system 1 showing all sub-system interactions.

A block diagram of the overall system is shown in Fig. 3. Each sub-system in the block diagram will be described in detail in its own sub-section. The system dynamics and force input transformation depicted are only used in simulation, and it in experimental trials, these sub-systems are physically realized.
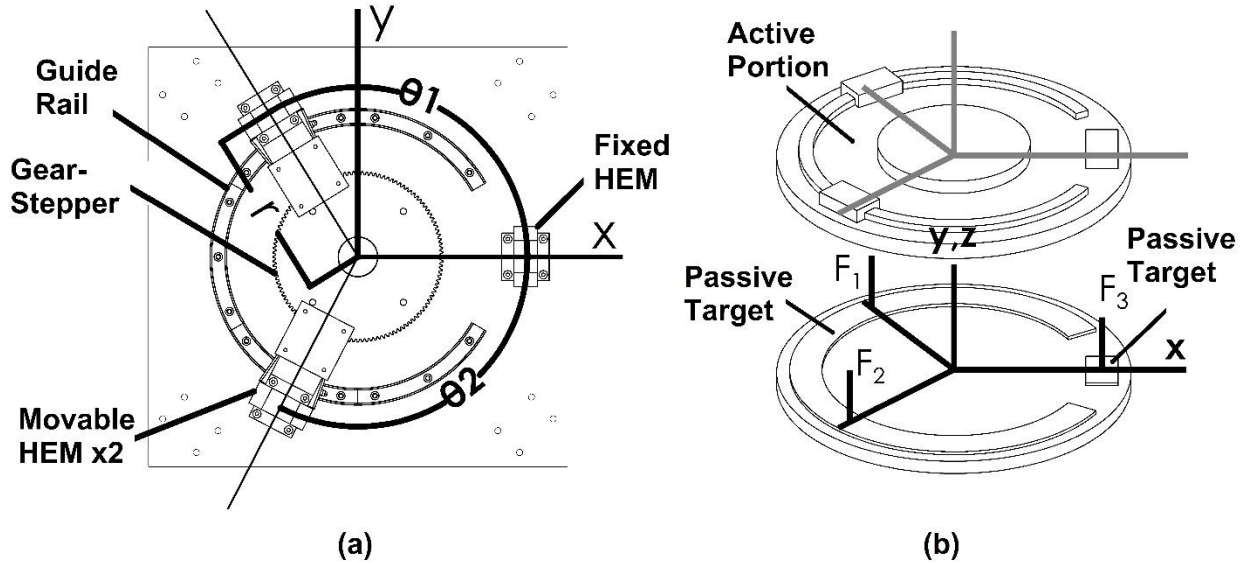
Fig. 4 – (a) An elevation view schematic and (b) perspective view schematic of system 1.

A schematic of system 1 is shown in Fig. 4. It can be seen that two HEMs are constrained to move about a circular guide rail while the third HEM is fixed. Two moving HEMs is the minimum number required to achieve active zero-power tip and tilt control. The centroid of the permanent magnets in system 1 can be determined by

$$\begin{Bmatrix} C_x \\ C_y \end{Bmatrix}_{S1} = \begin{Bmatrix} \frac{r}{3}(cos\theta_1 + cos\theta_2 + 1) \\ \frac{r}{3}(sin\theta_1 - sin\theta_2) \end{Bmatrix}. \tag{8}$$

It should be noted that the relationship between the centroid and the angular displacements is a non-linear one-to-one function for $0 < \theta_1, \theta_2 < 180$ degrees. In application, the inverse function to (8) is calculated by a look-up-table.

1a. Displacement Controller
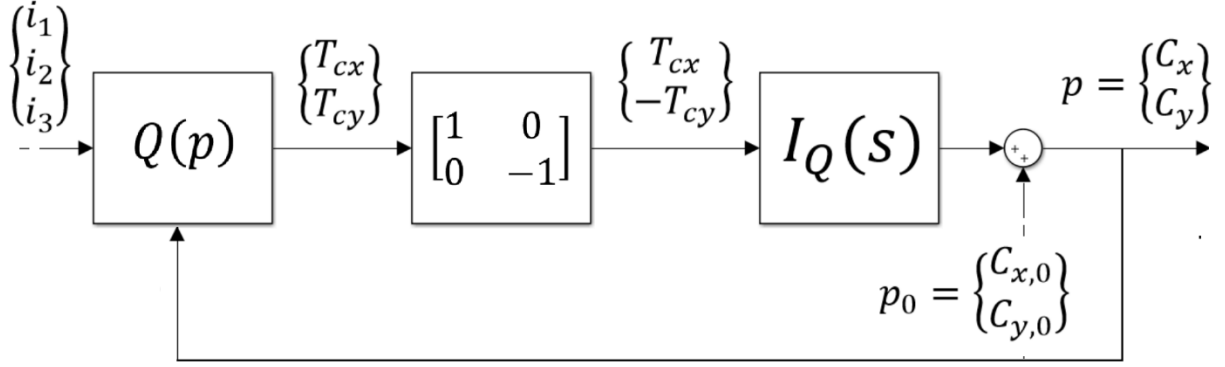
Fig. 5. – A block diagram depicting the displacement controller.

A block diagram depicting the displacement controller is shown in Fig. 5 where it can be seen that the centroid command $\{C_x, C_y\}'$ is dependent on the current centroid location. For system 1, the transformation Q defined in (5) is given as

$$Q_{S1} = -\begin{bmatrix} 0 & k_{I,Disp} \\ -k_{I,Disp} & 0 \end{bmatrix} \begin{Bmatrix} rsin\theta_1 - Cy, -rsin\theta_2, -Cy, -C_y \\ -rcos\theta_1 + C_x, -rcos\theta_2 + C_x, -r + C_x \end{Bmatrix}_{S1}, \tag{9}$$

where k_i and k_z have been replaced with the integrator gain $k_{I,Disp}$. The relationship between the permanent magnet centroid that creates a moment in the direction opposite to the moment generated by the active currents is given by

$$\begin{Bmatrix} C_x \\ C_y \end{Bmatrix}_{S1} = Q_{S1} \begin{Bmatrix} i_1 \\ i_2 \\ i_3 \end{Bmatrix}_{S1}. \tag{10}$$

By integrating $\{C_x, C_y\}_{S1}'$ as depicted in the block diagram in Fig. 5, the zero-power centroid location can be converged on.

1b. Air-gap Controller
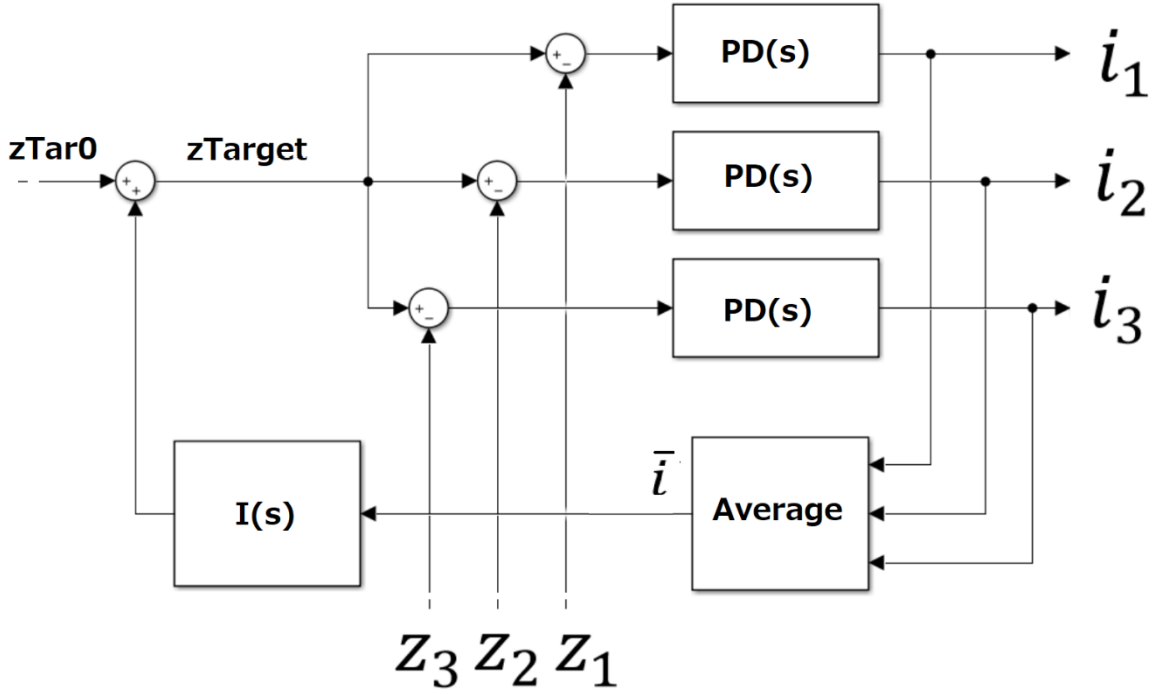
Fig. 6. – A block diagram depicting the air-gap controller.

A block diagram of the air-gap controller is shown in Fig. 6. In this controller, local positional-differential (PD) control is employed at each HEM independently. The input for each PD controller is the error between the target air-gap and the actual air-gap. When the system starts at its unloaded zero-power equilibrium, the target air-gap is given by

$$z_{Tar,S1}(s) = \frac{k_{Igap,S1}}{s} \tag{11}$$

where the input to (11) is the average current as a function of time $\bar{\imath}_{S1}(t)$. The target described in (11) is used for simulations, however to improve system performance during experimental trials, a different target is used which takes the form

$$z_{Tar,Exp}(s) = z_{Tar,S1}(s) + I_E(s). \tag{12}$$

where the function

$$I_E(s) = \frac{k_{Im}}{s} \tag{13}$$

11

is a function with the input of local air-gap minus average air-gap $\bar{z}(t) - z_n(t)$. The target described in (12) ensures that the system remains level while minimizing average current draw.

2. Simulation

Mathematical formulations and simulation results are presented in this section.

2a. System Dynamics Formulation
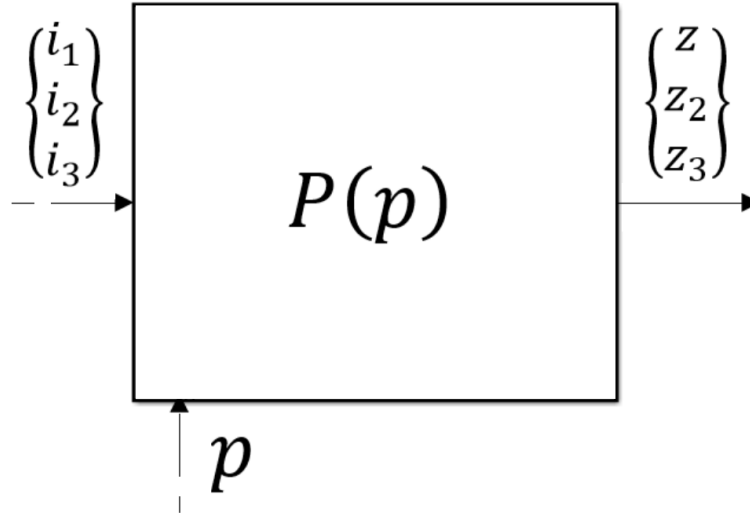
Fig. 7 – A block diagram depicting the system dynamics used for simulation.

For simulation, the system dynamics of the levitated platform are modeled as a linear parameter varying (LPV) system which linearly interpolates between linear state-space models depending on a scheduling parameter p. The general form for an LPV system is given as

$$dx(t) = A(p)x(t) + B(p)u(t) \tag{14}$$
$$y(t) = C(p)x(t) + D(p)u(t), \tag{15}$$

where the designation $P(p)$ is assigned to the system described in this section which consists of state space model ABCD and is dependent on the scheduling parameter $p = \{C_y, C_x\}$.

The formulation of the state space model starts with the equations of motion, which have been written to separate the z-height and i-current contributions

$$M \begin{Bmatrix} \ddot{z} \\ \ddot{\alpha} \\ \ddot{\beta} \end{Bmatrix} = \begin{Bmatrix} F_z \\ M_x \\ M_y \end{Bmatrix}_z + \begin{Bmatrix} F_z \\ M_x \\ M_y \end{Bmatrix}_i , \tag{16}$$

where

$$M = \begin{bmatrix} m & 0 & 0 \\ 0 & I_x & 0 \\ 0 & 0 & I_y \end{bmatrix}, \tag{17}$$

Next, a transform is defined between the force F_n at each HEM and an equivalent force and torque about the origin

$$\begin{Bmatrix} F_z \\ T_x \\ T_y \end{Bmatrix} = T \begin{Bmatrix} F_1 \\ F_2 \\ F_3 \end{Bmatrix}, \tag{18}$$

where

$$T = \begin{bmatrix} 1 & 1 & 1 \\ r\sin\theta_1 & -r\sin\theta_2 & 0 \\ -r\cos\theta_1 & -r\cos\theta_2 & -r \end{bmatrix}. \tag{19}$$

It follows that

$$\begin{Bmatrix} \delta z_1 \\ \delta z_2 \\ \delta z_3 \end{Bmatrix} = T' \begin{Bmatrix} \delta z \\ \delta\alpha \\ \delta\beta \end{Bmatrix}. \tag{20}$$

Linearizing about the system's unloaded zero-power equilibrium where the weight of the system equals the total attractive magnetic force from the HEMs yields the model with zero initial conditions

$$\begin{Bmatrix} \ddot{z} \\ \ddot{\alpha} \\ \ddot{\beta} \end{Bmatrix} = M^{-1} k_z T T' \begin{Bmatrix} z \\ \alpha \\ \beta \end{Bmatrix} + M^{-1} k_i T \begin{Bmatrix} i_1 \\ i_2 \\ i_3 \end{Bmatrix}, \tag{21}$$

where k_z and k_i are linearized force stiffness constants for air-gap and current respectively.

It should be noted that a linearized force profile is used here as previous research has shown that such a profile is sufficient for simulations for robust, level levitation [5,13-14]. Further, during level levitation, the non-linear nature of a more accurate force profile does not negatively influence differential current feedback as the air-gaps and the passive attractive forces at each HEM are equivalent.

13

Continuing, the state variable is defined as

$$X = [z, \alpha, \beta, \dot{z}, \dot{\alpha}, \dot{\beta}\,]' \tag{22}$$

and the state space realization of the form given in (3) and (4) becomes

$$A(p) = \begin{bmatrix} 0_{3x3} & I_{3x3} \\ M^{-1}k_z TT' & 0_{3x3} \end{bmatrix} \tag{23}$$

$$B(p) = \begin{bmatrix} 0_{3x3} \\ M^{-1} k_i T \end{bmatrix} \tag{24}$$

$$C(p) = [T', 0_{3x3}] \tag{25}$$

$$D(p) = [0_{3x3}, 0_{3x3}], \tag{26}$$

where the input and output are respectively

$$u(t) = \begin{Bmatrix} i_1 \\ i_2 \\ i_3 \end{Bmatrix} \tag{27}$$

$$y(t) = C(p)x(t) = \begin{Bmatrix} z_1 \\ z_2 \\ z_3 \end{Bmatrix}. \tag{28}$$

Checking the observability and controllability matrices yields that they are full rank and that the system is both state controllable and observable for all non-singular angle pairs in a single period $\theta_1 \neq \theta_2$. Although in general the LPV system $P(p)$ is non-linear, a linearized transfer function of can be given for a constant scheduling parameter p as

$$P_p(s) = C(sI - A)^{-1}B + D. \tag{29}$$
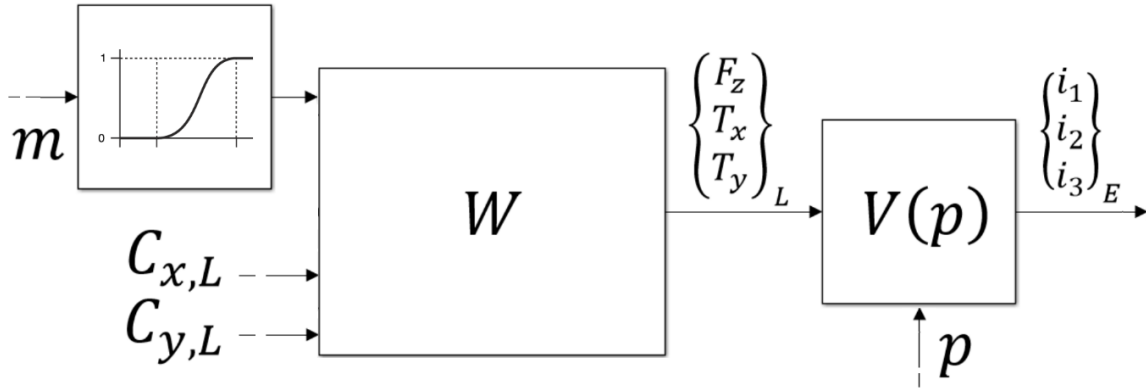
Fig. 8 – A block diagram of the force input transformation used in simulation.

Because the system is parameter varying, a force input transformation is required to input static forces into the system dynamics. The block diagram for the force input transform is shown in Fig. 8. An equivalent force and torque caused by an eccentric mass which results in the overall center-of-mass of the system $\{C_{x,L}, C_{y,L}\}$ can be given as

$$
\begin{Bmatrix} F_z \\ T_x \\ T_y \end{Bmatrix}_L = \begin{Bmatrix} -m_L g \\ -m_L g C_{y,L} \\ m_L g C_{x,L} \end{Bmatrix}, \tag{30}
$$

where the subscript L denotes an external load. This load can then be converted into an equivalent current and added as an input to the system dynamics. This transformation is given by

$$
\begin{Bmatrix} i_1 \\ i_2 \\ i_3 \end{Bmatrix}_E = V(p) \begin{Bmatrix} F_z \\ T_x \\ T_y \end{Bmatrix}_L \tag{31}
$$

where

$$
V(p) = \frac{1}{k_i} T^{-1}. \tag{32}
$$

The system dynamics in (21) can then be rewritten to include the converted load as

$$
\begin{Bmatrix} \ddot{z} \\ \ddot{\alpha} \\ \ddot{\beta} \end{Bmatrix} = M^{-1} k_z T T' \begin{Bmatrix} z \\ \alpha \\ \beta \end{Bmatrix} + M^{-1} k_i T \begin{Bmatrix} i_1 + i_{1E} \\ i_2 + i_{2E} \\ i_3 + i_{3E} \end{Bmatrix} \tag{33}
$$

or alternatively as

$$
\begin{Bmatrix} \ddot{z} \\ \ddot{\alpha} \\ \ddot{\beta} \end{Bmatrix} = M^{-1} k_z T T' \begin{Bmatrix} z \\ \alpha \\ \beta \end{Bmatrix} + M^{-1} k_i T \left(\begin{Bmatrix} i_1 \\ i_2 \\ i_3 \end{Bmatrix} + \begin{Bmatrix} F_z \\ T_x \\ T_y \end{Bmatrix}_L \right). \tag{34}
$$

It should be noted that although this force conversion neglects inertial effects, it is suitable for typical simulations of suspended masses where both translational and angular accelerations are expected to be negligibly small. Further, in the steady-state, inertial effects are not present and accurate zero-power convergence can be attained.

In simulation, rather than using a traditional unit step input, a unit smooth-step input is used to represent the eccentric mass being placed on the platform. The unit smooth-step is mathematically defined as the double integral of a single period of a square sine wave where the amplitude is four times the inverse of the period squared. A smooth-step better represents how a mass would be placed on the platform in the physical world and serves to reduce high frequency vibrations in the simulation.

2b. Scheduling and Interpolation

In simulations, all functions of the scheduling parameter p require scheduling and linear interpolation. The scheduling resolution and range are outlined in the Table 2. The scheduling range was chosen as an engineering compromise which allows for robust levitation [8]. In certain spaces outside of the selected range, large moments become difficult to realize due to the HEMs becoming too close, reducing the length of the moment generating torque arm. In other spaces, configurations are not physically achievable due to spatial overlap.

Table 2 – System 1 Simulation Parameters

Symbol	Parameter	Value
Res	Resolution	10
---	Centroid Upper Bound	$\sqrt{2}/12$ (m)
---	Centroid Lower Bound	$-\sqrt{2}/12$ (m)
---	Simulink Solver	Ode(45)
---	Simulink Max Step Size	0.001 (s)
---	Smooth-Step Time	0.0 (s)
---	Smooth-Step Duration	0.2 (s)
k_i	Force-Current stiffness	10 (N/A)
k_z	Force-Height stiffness	10,000 (N/m)
K_P	Proportional Gain	5,000
K_I	Integral Gain, Levitation	1/200
K_D	Derivative Gain	125
N	Filtering Coefficient	500
m	Mass of Unloaded System	2 (Kg)
I_x	Unloaded Moment of Inertia, x	0.5 (Kg m^2)
I_y	Unloaded Moment of Inertia, y	0.5 (Kg m^2)
r	Radius of HEMs	1 (m)

	C_y Low	.	.	.	C_y High
C_x Low	Data (1,1)	.	.	.	Data $(Res, 1)$
.		.	.		
.		.		.	
.		.			.
C_x High	Data $(1, Res)$				Data (Res, Res)

Fig. 9. A graphic depiction of the lookup table used for linear model interpolation.

A visual representation of the scheduling grid from which state-space models are linearly interpolated between is shown in Fig. 9. As some of the relationships that require scheduling are highly non-linear, only interpolation is conducted. Cases in which the scheduling parameter *p* exceeds the selected range are therefore invalid.

2c. Parameter Tuning

Table 3 – System 1 Displacement Controller Parameters

Symbol	Parameter	Value
m_L	Load Mass	5 (Kg)
K_Q	Integral Gain, Orientation	0, 1/25, 1
$\{C_{x,L}, C_{y,L}\}$	Load Center of Mass	$\{0.1, 0.1\}$ (m)

Table 3 defines the simulation parameters which resulted in the data presented in Figs. 10-12. As the displacement controller integral gain K_Q is directly related to the mass of the load, the same trends would be observed when varying the mass with a constant gain as when varying the gain with a constant mass.

2d. Simulation Results
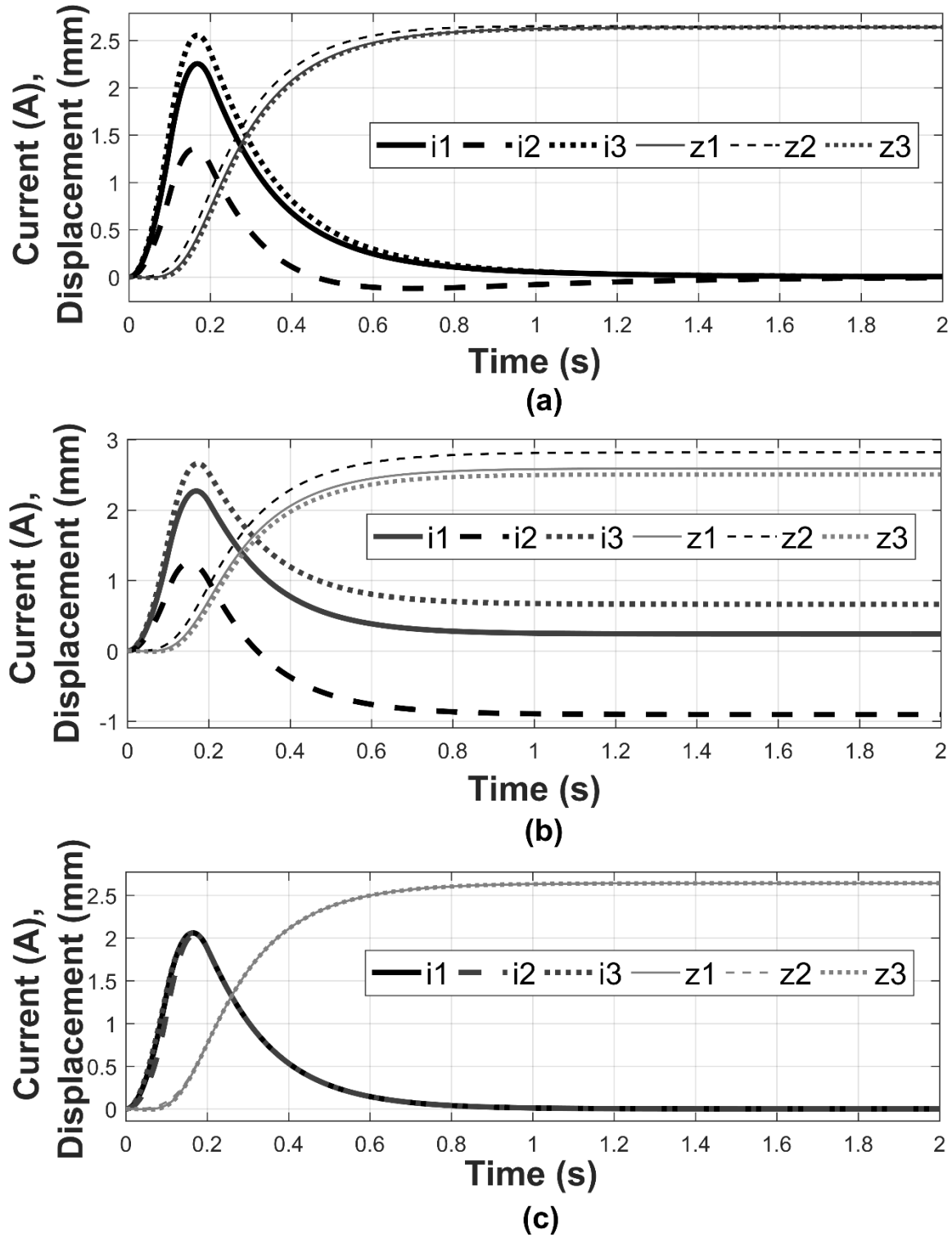
Fig. 10. – Simulation results using the parameters defined in Table II are shown for $K_Q=1/25$, 0, and 1 in subplot (a), (b), and (c), respectively.
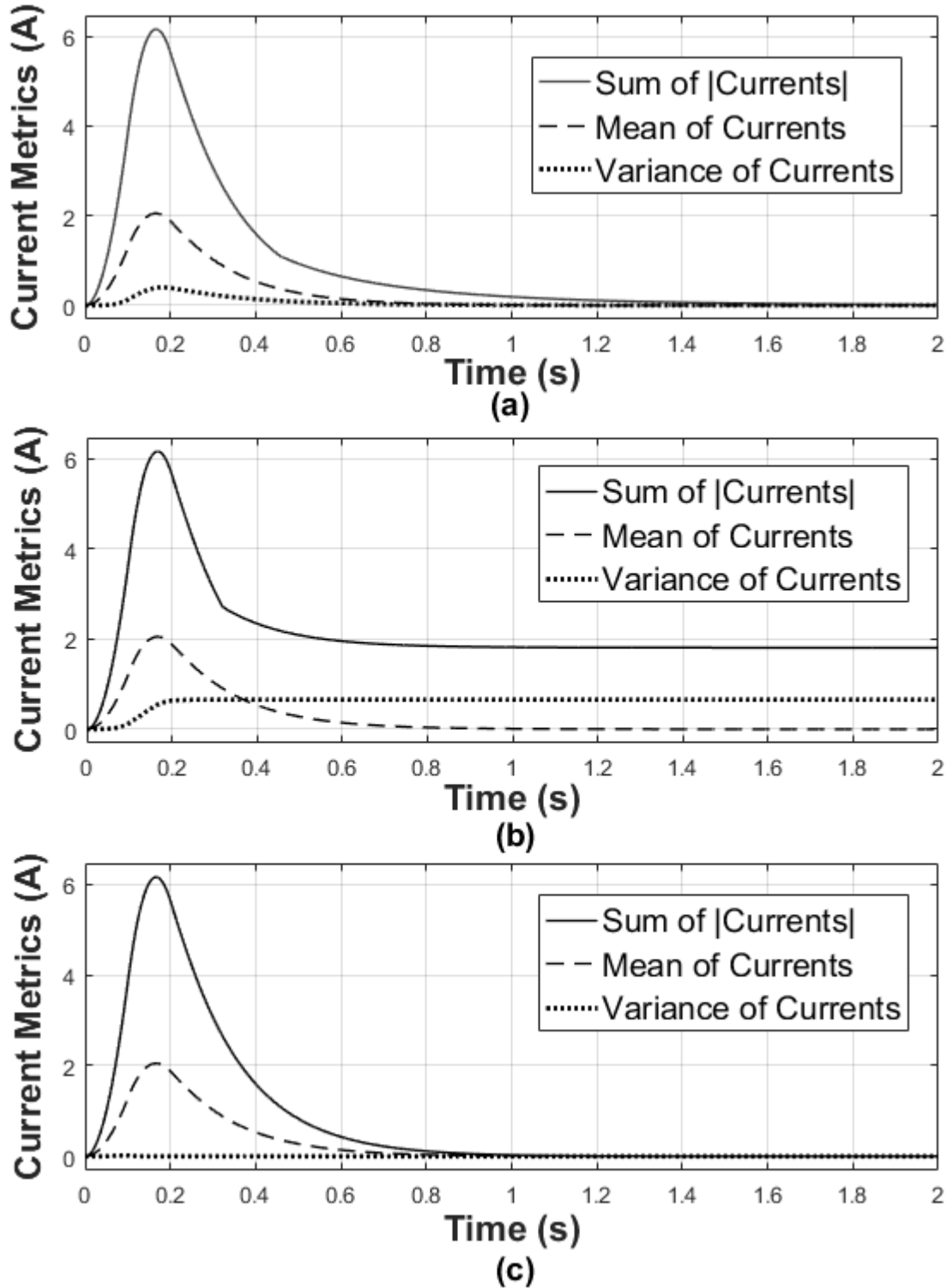
Fig. 11. Simulation results using the parameters defined in Table II are shown for $K_Q = 1/25$, 0, and 1 in subplot (a), (b), and (c), respectively. The derivative discontinuity in the sum of the absolute value of the currents is attributed to the absolute value being a piecewise function.
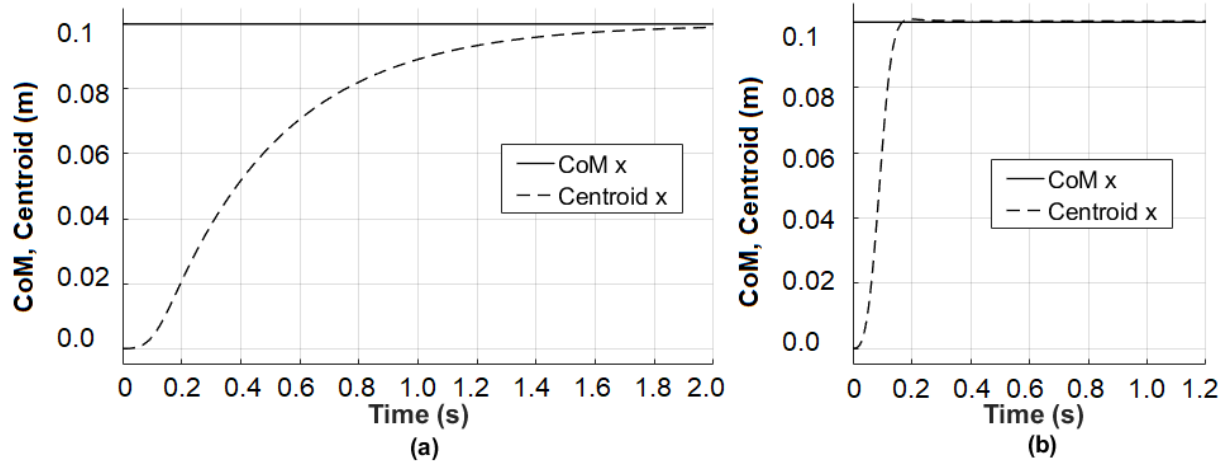
Fig. 12. Simulation results using the parameters defined in Table II are shown for $K_Q=1/25$ and 1 in subplot (a) and (b) respectively. As x and y data is identical, so only x data is shown for clarity. The response time of 0.2s achieved in (b) is difficult to achieve in physical systems.

For the results in Figs. 10-12 it should be recalled that force is applied in a smooth-step from time=0 to 0.2 seconds. Fig. 10 depicts current and z-position data versus time for $K_Q=1/25$, 0, and 1 in subplots (a), (b), and (c) respectively. In Fig. 10(a), it can be seen that zero-power is achieved in approximately 2 seconds. Although convergence occurs faster in Fig 10(c), this result is difficult to realize in physical systems as it requires rapid acceleration of the HEMs as is shown in Fig. 12. In Fig. 10(b), the operation of the system without the displacement controller, e.g. $K_Q=0$, is shown. As expected, it can be noted that in this case that the z-heights of HEMs do not converge to a single value as each locally controlled HEM does not have an independent integrator. In Fig. 11(b) it can be verified that the mean current converges to zero, however, the sum of the absolute value of current does not. Further, in Fig. 11(b) it can be seen that after a transient period, the variance of currents remains constant, which is expected when the displacement controller is disabled. In Fig. 11(c) it can be seen that with a sufficiently large integral gain, the variance in currents can be maintained at nearly zero. This suggests that performance of the tip-tilt control method is hardware limited, and can be improved if the HEMs can be made to accelerate faster.

3. Hardware
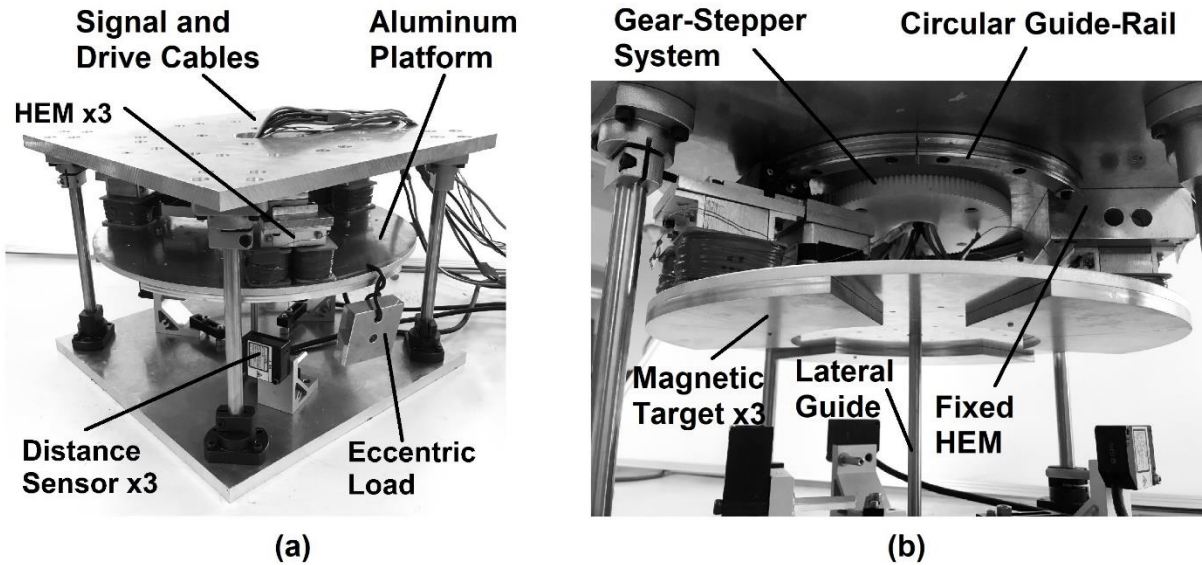
Fig. 13. – (a) Photogrpah of hardware from slightly elevated view with key components indicated. (b) Photograph of hardware from slightly deelevated view with key components indicated.

A photograph of the system 1 hardware is depicted in Fig. 13. The method of suspending the eccentric mass on the platform is depicted in Fig. 13(a). For clarity, elevated and elevated views are given in Fig. 13(a) and Fig. 13(b) respectively. The relevant hardware parameters for system 1 are tabulated in Table 4.

Table 4 – Hardware Parameters

Parameter	Value
Permanent Magnet Dimensions	18 x 39 x 25.4 (mm)
Magnetization Direction Dimension	25.4 (mm)
Permanent Magnet Material	Neodymium N50
Total Number of Coil Windings	720 turns
HEM Pole material	SS400
Minimum Stepper Resolution	9/320 (degrees/step)
Platform Mass	1.75 (Kg)
Platform Diameter	0.3 (m)
Eccentric Load Mass	0.25 (Kg)
Eccentric Load Coordinates {x, y}	{0, -0.3} (m)

The force profiles for the HEMs is roughly characterized

$$F_f = 44.95 \left(\frac{i_f + 6.83}{z_f + 3.41} \right)^2, \tag{35}$$

where F_f is in Newtons, i_f is in Amperes, and z_f is in millimeters. This force profile was created through a curve fitting and is given for the edification of the reader. The curve fitting data was not necessary for controller tuning. Fig. 14 shows the empirical points used for curve fitting.
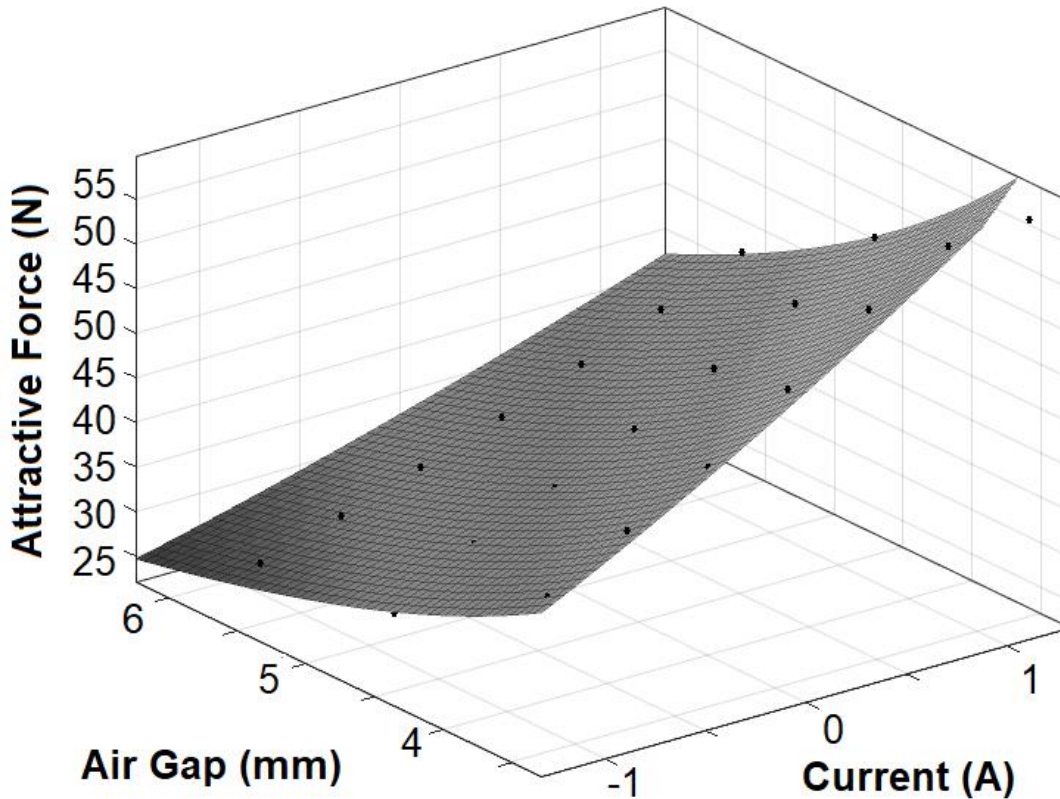
Fig. 14. Force profile for the HEMs as determined by the curve fitting of emperical data. Inaccuracies are expected to raise when extrapolating the data and when accounting for unpredicted flux losses to adjacnet hardware components.

As system 1 is only considered in 3 DoF, a lateral guide pole is inserted through a hole in the platform to constrain lateral motion of the platform as is shown in Fig. 13(b). However, the tolerance of this guide still allows for free rotation in the z-direction and roughly five millimeters of lateral travel. It was observed experimentally that lateral translation rotation of the levitated platform caused unwanted vibrations and negatively impacted the performance of the system.

4. Experimental Procedure

The hardware calibration and experimental procedure for each of the conducted trials is described in this section. An overview of the conditions of the conducted trials is tabulated in Table 5. A written description is given for each trial in its respective sub-subsection.

Table 5 – System 1 Summary of Experimental Trials

	Trial Name	Eccentric Load Placed	ZP Tip-Tilt Control
Trial 1	Horizontal Pre-Load	Before t=0	After t=0
Trial 2	Horizontal Post-Load	After t=0	Before t=0

A summary of the relevant parameters used commonly in all trials is tabulated in Table 6.

Table 6 – System 1 Summary of Experimental Timings

Trial Number	Condition	Value
1	Displacement Controller Activation Timing	t=10 (s)
1	Approximate Settling Time	15 (s)
2	Eccentric Load Application Timing	t=20 (s)
2	Approximate Settling Time	20 (s)

4a. Calibration

For each experimental trial, the laser distance sensors are recalibrated such that they read zero distance when the HEMs are in contact with the magnetically permeable target. The angular starting position of the HEMs is determined geometrically, where a physical stopper is used to locate the HEMs with respect to the circular guide rail. It is expected that due to manufacturing imperfections, the starting angular locations of the HEMs are not exactly 120 degrees apart from each other. However, from experimental data, it was seen that zero-power convergence was still achievable to the resolution of the sensing hardware.

4b. Horizontal Pre-Load Trial

In the horizontal pre-load trial, the eccentric mass is placed on the system and the system is allowed to reach steady state elevated equilibrium before time t=0. After a short period of stead-state levitation, the displacement controller is activated and the HEMs are angularly displaced by the controller around the circular guiderail. The system is then allowed to reach its new steady state equilibrium before the experimental trial is ended. The exact details of the trial are tabulated in Table 4 and Table 6.

4c. Horizontal Post-Load Trial

In the horizontal post-load trial, the system is allowed to levitate unloaded with the displacement controller activated before time t=0. After a short period of stead-state levitation, the eccentric mass is placed slowly by hand (approximately over the time period of 3 seconds) onto the levitated platform. The system is then allowed to reach its new steady state equilibrium before the experimental trial is ended. The exact details of the trial are tabulated in Table 4 and Table 6.

5. Experimental Data

The data from the pre-loaded trial is meant to emphasize the current draw reduction gained by the displacement controller, while the post-loaded trial is meant to exemplify the intended typical operation of system 1.

5a. Data Processing

During the conducted experimental trails, unwanted lateral translations of the system resulted in unwanted vibrations and noise in the collected data. As such, the experimental current and height data presented is down-sampled to allow the dynamic and steady-state trends be more clearly seen. The HEM angle data is presented in full resolution. Down-sampling was conducted by averaging 20,000-sample batches into a single data point which is then graphically represented at the end of each batch. For the edification the reader, the down-sampled HEM 1 data for horizontal pre-loaded trial is compared to the raw data of the same trail in Fig. 15. As the raw data for all six channels in both trials was deemed unclear and unbeneficial, it was elected to only present the down-sampled data.
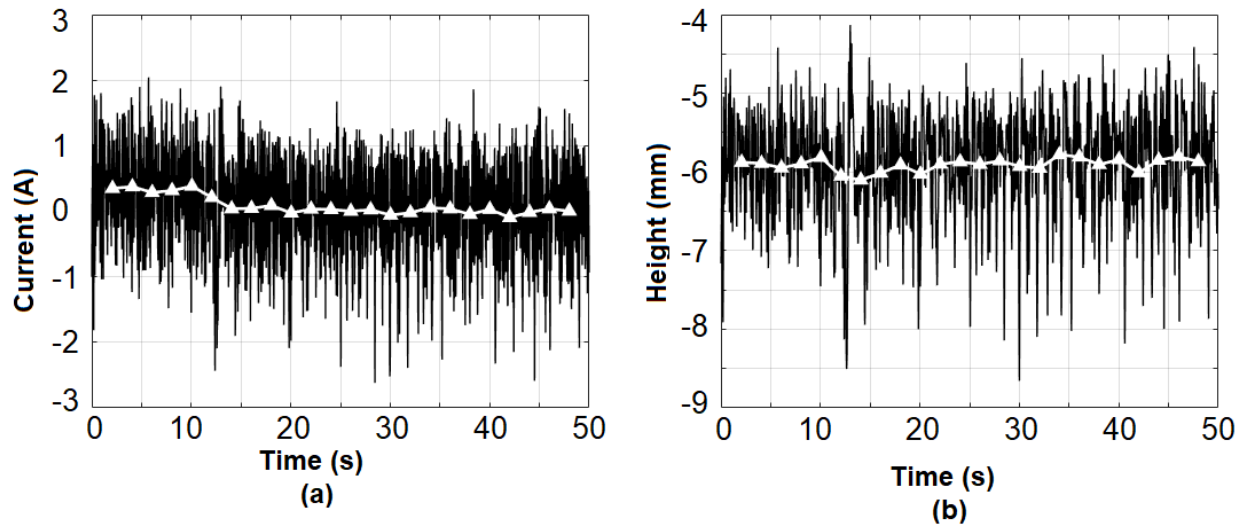
Fig. 15. – Down-sampled data overlaid over raw data for HEM 1 during the pre-loaded trail. The down-sampled data can be visually verified to be identical to HEM 1 data in Fig. 17.

5b. Horizontal Pre-Load Trial

The experimental data for the horizontal pre-loaded trial is depicted in Fig. 16. Here, the displacement controller was activated after 10 seconds as is indicated by the arrow in Fig. 16(c). It can be seen in Fig. 16(a) that prior to the activation of the displacement controller, the system is in its steady-state, however, the variance of current is not zero. This is the expected result as previously determined by simulation. After the displacement controller is activated, it is confirmed that the mean and variance of currents converges to zero after roughly 20 seconds. In Fig. 16(b) it can be seen that immediately after the displacement controller is activated, the height of HEM 1 dips while height of HEM 2 raises. This data expresses roughly that the platform tilted about its geometric center in the direction opposite to the direction of moment caused by the eccentric mass. Also in Fig. 16(b), it can be seen that the steady-state z-height of platform before and after the activation of the displacement controller is approximately the same, validating the interpretation that the air-gap controller is responsible for minimizing the mean of currents and the displacement controller is responsible for minimizing the variance of currents.
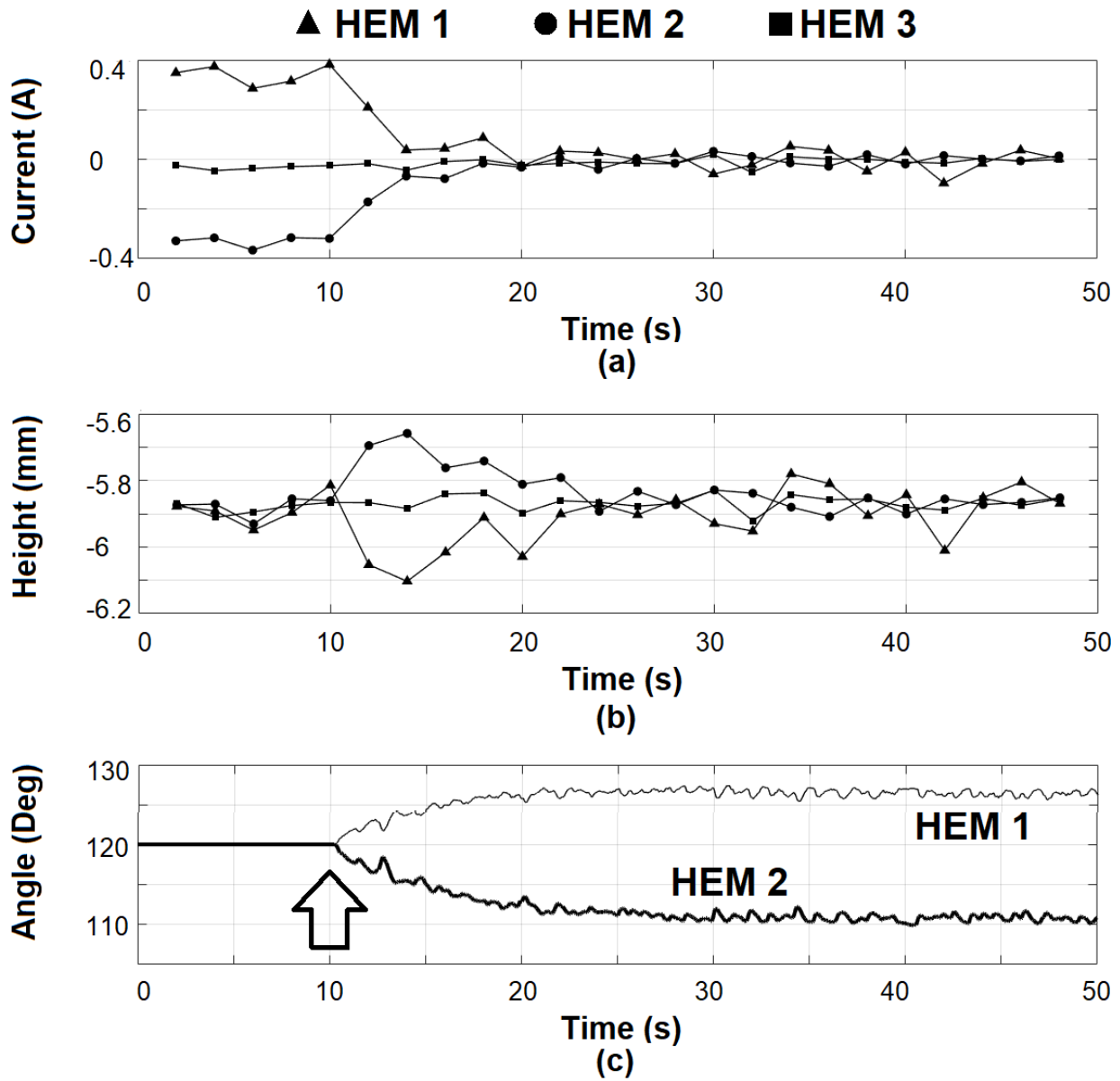
Fig. 16 – Data from the pre-loaded trial where the displacement controller is activated at 10 second as indicated by the arrow. (a) Down-sampled current data. (b) Down-sampled height data. The air-gap between the HEM and the permeable target is 6mm less than the height of the platform due to the 6mm thickness of the aluminum platform itself. (c) Full resolution angle data. It can be seen that the system reaches steady state after approximately 20 seconds.

5c. Horizontal Post-Load Trial

The experimental data for the horizontal post-loaded trial is depicted in Fig. 17. Here, the eccentric mass was gently applied by hand after roughly 20 seconds as indicated by the arrow in Fig. 17(c). It can be seen in Fig. 17(a) that prior to the application of the eccentric mass, the system is steady-state, but the HEM angles have converged to a value other than 120 degrees. This result can be attributed to imperfections in manufacturing, differences the in the HEMs' permanent magnets, and to the five millimeter lateral freedom of the platform. The slight difference between the loaded steady-state HEM angles in the pre-loaded and post-loaded trials can also be attributed to these same errors.

In Fig. 17(b) it can be seen that the zero-power z-height is increased after the load is added and it can be observed that steady-state is achieved after approximately 10 seconds. Immediately after the eccentric load is placed, it can be seen that the height of HEM 2 decreases more than HEM 1 indicating that the platform has tilted in the same direction as the moment caused by the eccentric load. It can also be seen that immediately after placing the eccentric mass, a higher current magnitude is required at HEM 2 as compared to HEM 1.
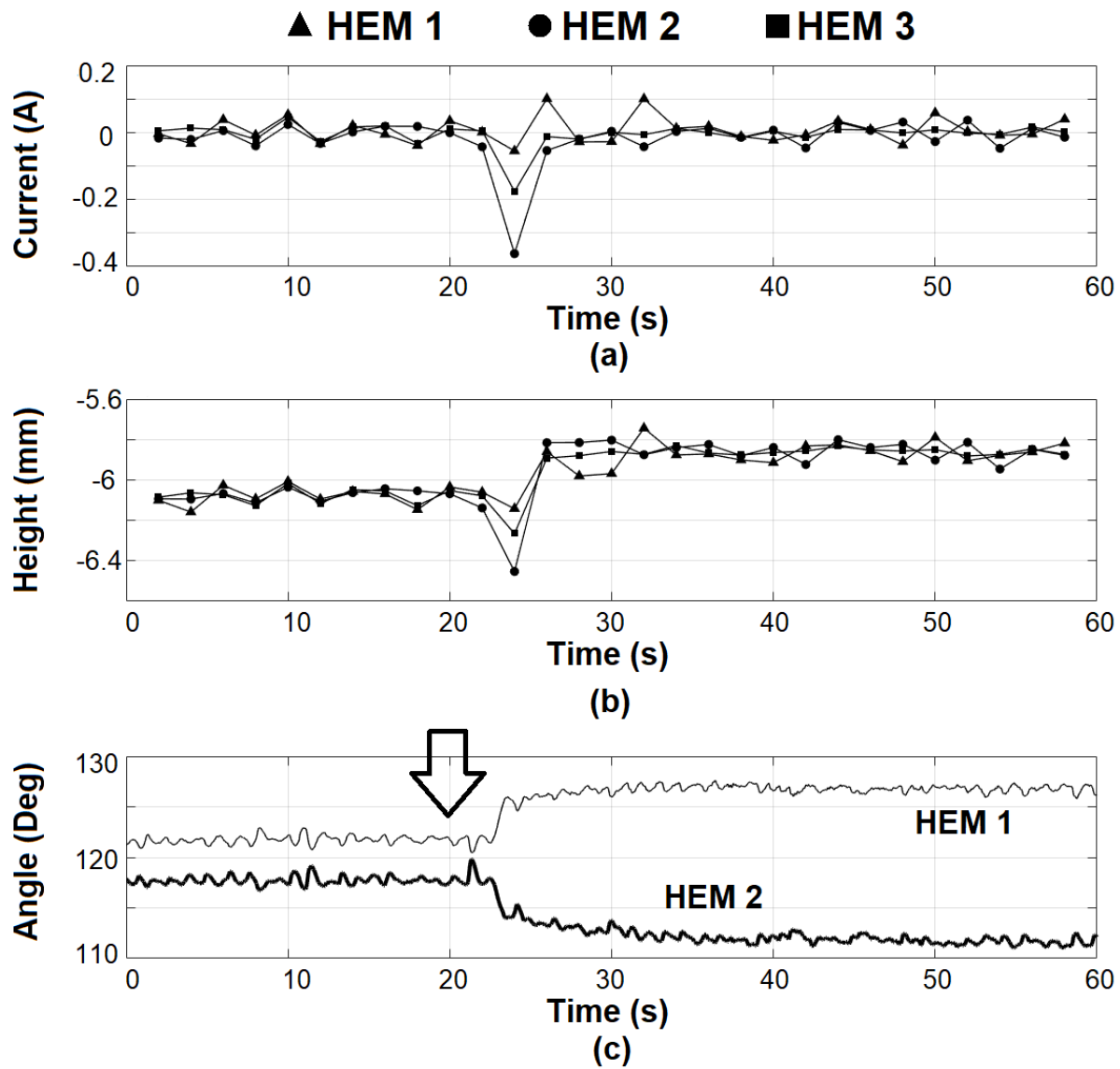
Fig. 17 – Data from the post-loaded trial where the eccentric mass is added gently by hand after roughly 20 seconds as indicated by the arrow (a) Down-sampled current data. (b) Down-sampled height data. The air-gap between the HEM and the permeable target is 6mm less than the height of the platform due to the 6mm thickness of the aluminum platform itself. (c) Full resolution angle data. It can be seen that the system reaches steady state after approximately 15 seconds.

28

Chapter 4 – System 2

1. Mathematical Formulation
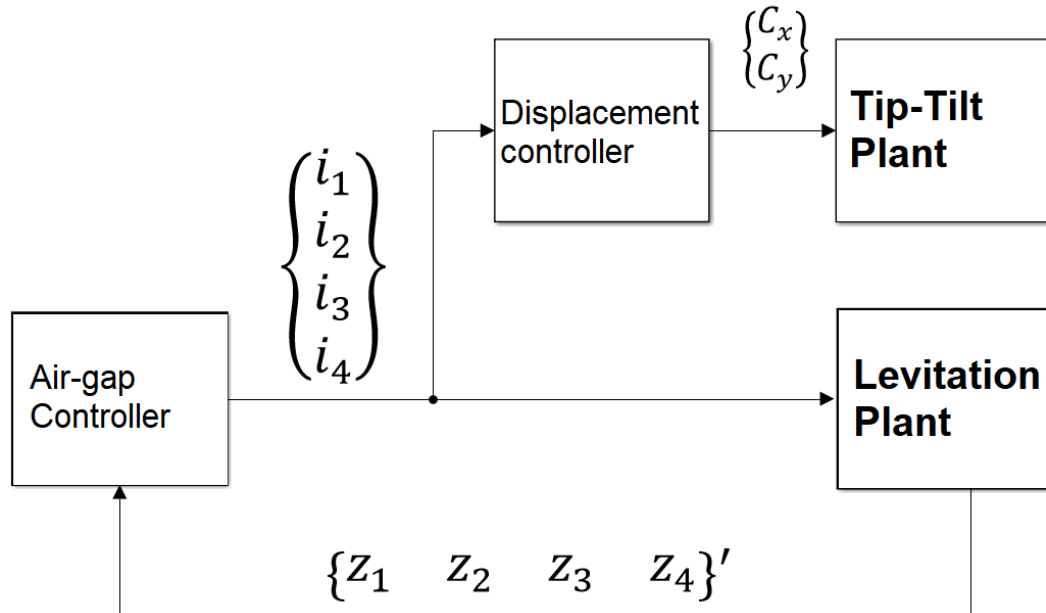
Fig. 18 – A block diagram depicting the sub-system interactions in system 2.

The mathematic formulation for system 2 is conducted in this section. A block diagram of the overall system is shown in Fig. 18. Each sub-system in the block diagram will be described in detail in its own sub-section.

A schematic of the zero-power tip-tilt system is shown in Fig. 19 where the reference frame has been indicated. It should be noted that the configuration of tip-tilt system is not unique. The configuration depicted in Fig. 19 was selected for easy of manufacturing and for its application to linear and planar sliders [15-17]. In the case of a slider any number of linear actuators could be used to achieve lateral acceleration the levitated platform [18-20].
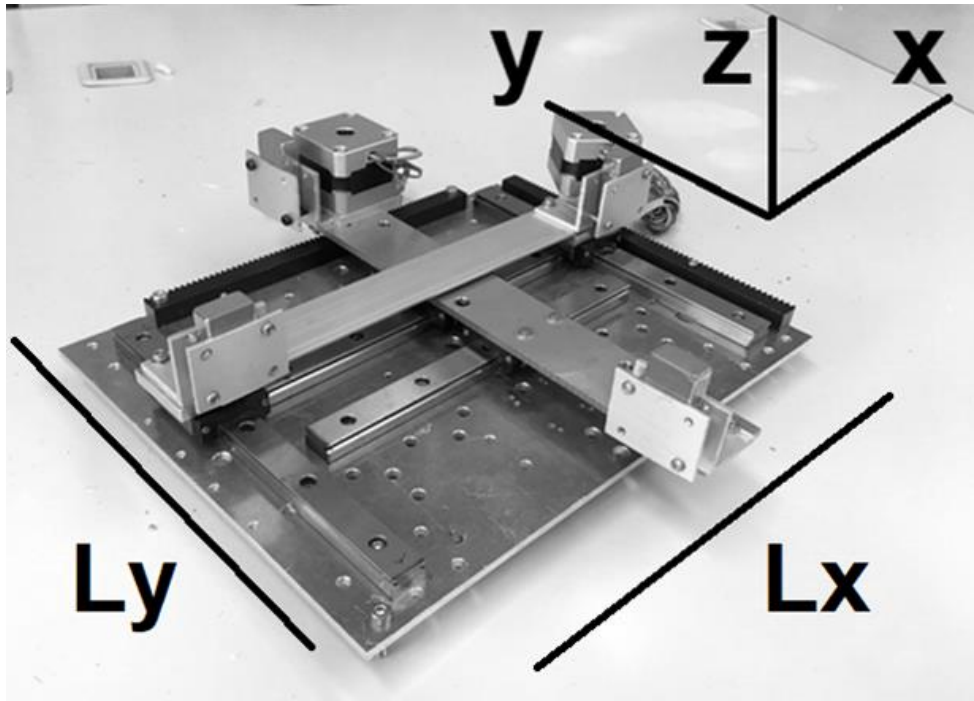
Fig. 19 – Photograph of isolated magnetic displacement system with reference frame indicated.

The centroid of the permanent magnets in system 2 can be determined by

$$\begin{Bmatrix} C_x \\ C_y \end{Bmatrix}_{S2} = \begin{Bmatrix} \frac{1}{2}c_x \\ \frac{1}{2}c_y \end{Bmatrix} \tag{36}$$

where c_x and c_x are the locations of the permanent magnet pairs in x and as is depicted in Fig. 19. It should be noted this relationship is linear, whereas the centroid relationship for system 1 is non-linear.

1a. Displacement Controller

$$\mathbf{Q} = \begin{bmatrix} k_{ICx} & k_{ICx} & -k_{ICx} & -k_{ICx} \\ -k_{ICy} & k_{ICy} & -k_{ICy} & k_{ICy} \end{bmatrix}$$

$$\begin{Bmatrix} i_1 \\ i_2 \\ i_3 \\ i_4 \end{Bmatrix} \rightarrow \boxed{k_i T_c} \rightarrow \begin{Bmatrix} M_x \\ M_y \end{Bmatrix}_{Lev} \rightarrow \boxed{\begin{bmatrix} 0 & k_{Ix} \\ -k_{Iy} & 0 \end{bmatrix}^{-1}} \rightarrow \boxed{\dfrac{1}{s}} \rightarrow \begin{Bmatrix} C_x \\ C_y \end{Bmatrix}$$
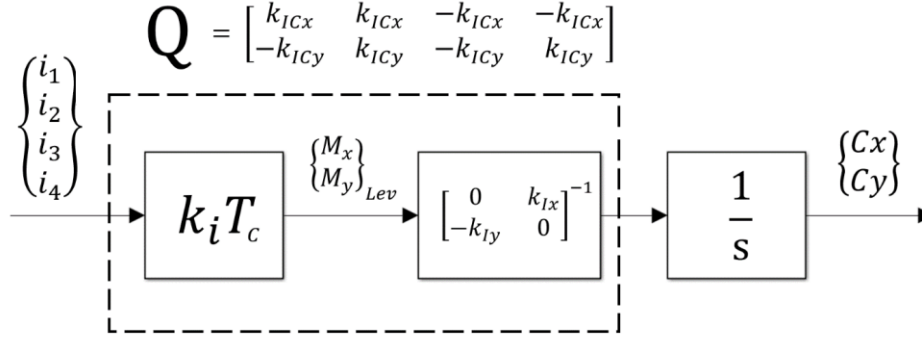
Fig. 20 – A block diagram depicting the displacement controller.

A block diagram of the displacement controller for system 2 is shown in Fig. 20. The input to the displacement controller can be seen to be currents $\{i_1, i_2, i_3, i_4\}'$ and the output can be seen to be the command displacement $\{C_x, C_y\}'$. For system 2, the transformation Q defined in (5) is given as

$$Q_{S2} = -\begin{bmatrix} 0 & k_{Iy} \\ -k_{Ix} & 0 \end{bmatrix}^{-1} k_i T_C = \begin{bmatrix} k_{ICx} & k_{ICx} & -k_{ICx} & -k_{ICx} \\ -k_{ICy} & k_{ICy} & -k_{ICy} & k_{ICy} \end{bmatrix} \tag{37}$$

where

$$T_C = \begin{bmatrix} -l_y & l_y & -l_y & l_y \\ -l_x & -l_x & l_x & l_x \end{bmatrix}. \tag{38}$$

Because Q_{S2} consists of only linear relationships, the constants relating to the dimesons of the system and to the magnetic strength l_y, l_y, and k_i can be replaced by two integral gains k_{ICx} and k_{ICy}. When this equivalent Q_{S2} is used with a feedforward integrator, the location of the permanent magnets in the displacement system will moved in the direction which reduces current variance.

To reiterate the basic principle of control discussed earlier, the moments caused by the displacement of permanent magnets

$$\begin{Bmatrix} M_x \\ M_y \end{Bmatrix}_{Displacement} = \begin{bmatrix} 0 & k_{Iy} \\ -k_{Ix} & 0 \end{bmatrix} \begin{Bmatrix} C_x \\ C_y \end{Bmatrix} \tag{39}$$

31

is used to counteract moments caused by active currents

$$\begin{Bmatrix} M_x \\ M_y \end{Bmatrix}_{Currents} = k_i T_C \begin{Bmatrix} \delta i_1 \\ \delta i_2 \\ \delta i_3 \\ \delta i_4 \end{Bmatrix}. \tag{40}$$

Because the relationships in (39) and (40) are linear, the only information which is inherited into equivalent transformation Q_{S2} in is the signage which are linked to the relative positions of the electromagnetic coils and magnets in the selected Cartesian reference frame.

1b. Air-gap Controller
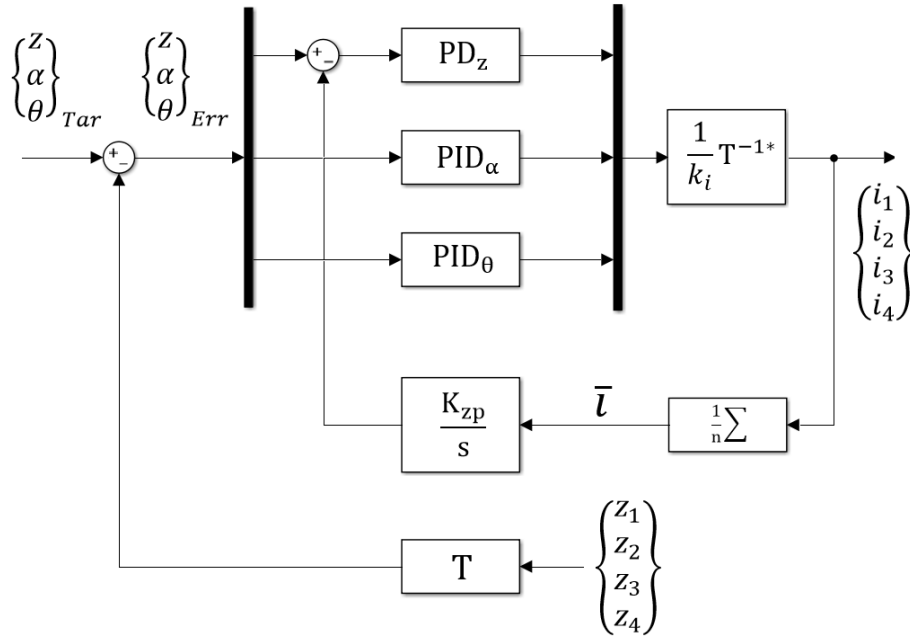
Fig. 21 – A block diagram depicting the air-gap controller.

A block diagram of the air-gap controller is shown in Fig. 21. This controller and its corresponding hardware was developed in previous research [5] and is given increased functionality in the present research. Only the critical aspects of the previously developed controller are explained here.

It can be seen in Fig. 21 that state-space control is employed where the state variable is $\{z, \alpha, \theta\}'$. The transform T_{S2} is developed between the feedback air-gap measurements and the state variable

32

$$\begin{Bmatrix} \delta z \\ \delta \alpha \\ \delta \theta \end{Bmatrix} = T_{S2} \begin{Bmatrix} \delta z_1 \\ \delta z_2 \\ \delta z_3 \\ \delta z_4 \end{Bmatrix}, \tag{41}$$

where

$$T_{S2} = \begin{bmatrix} -1 & -1 & -1 & -1 \\ -l_y & l_y & -l_y & l_y \\ -l_x & -l_x & l_x & l_x \end{bmatrix}, \tag{42}$$

and where l_x and l_y are the distances between the HEMs and the center of the platform in the x and y respectively.

A pseudo inverse T_{S2}^{-1*} is used to transform the command output $\{F_z, M\alpha, M_\theta\}'$ into the current command for the levitation plant $\{i_1, i_2, i_3, i_4\}'$

$$\begin{Bmatrix} \delta i_1 \\ \delta i_2 \\ \delta i_3 \\ \delta i_4 \end{Bmatrix} = \frac{1}{k_i} T_{S2}^{-1*} \begin{Bmatrix} \delta F_z \\ \delta M_\alpha \\ \delta M_\theta \end{Bmatrix}, \tag{43}$$

where,

$$T_{S2}^{-1*} = \begin{bmatrix} -\frac{1}{4} & -\frac{1}{4l_y} & -\frac{1}{4l_x} \\ -\frac{1}{4} & \frac{1}{4l_y} & -\frac{1}{4l_x} \\ -\frac{1}{4} & -\frac{1}{4l_y} & \frac{1}{4l_x} \\ -\frac{1}{4} & \frac{1}{4l_y} & \frac{1}{4l_x} \end{bmatrix}. \tag{44}$$

In the feed forward direction of the controller, it can be seen that a PD controller is used for the z state, while PID controllers are used for the α and θ states respectively. PIDs are used for the α and θ states for tracking the state target. A zero-power feedback integral loop is used with the PD controller for the z state to automatically adjusts the z target to minimize the mean of currents.

2. Hardware
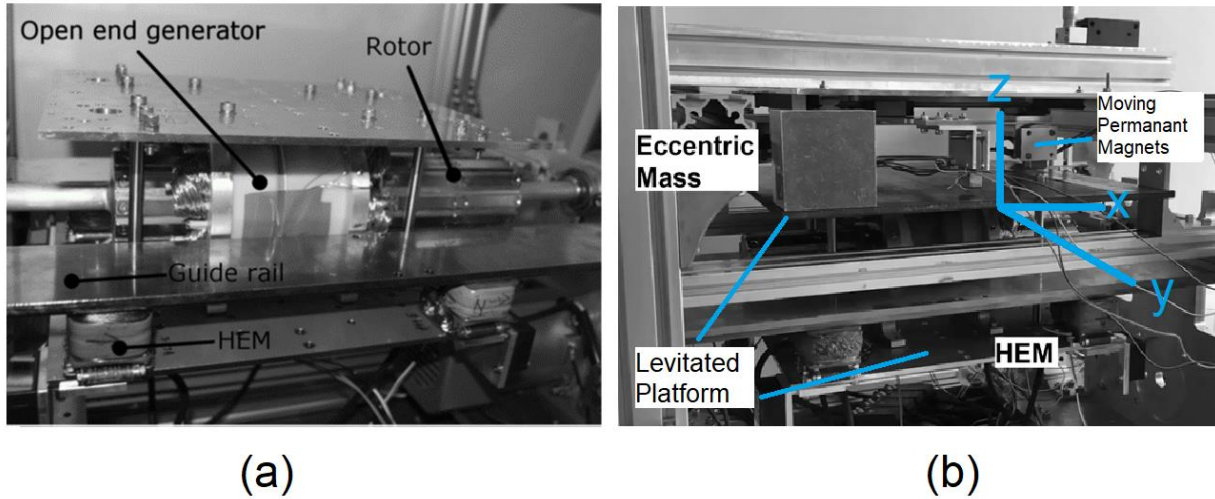
Fig. 22 – (a) Photograph of magnetically levitated linear slider isolated. The generator is not used in this research. (b) Photograph of integrated system consisting of permanent magnet displacement system and magnetically levitated linear slider.

A photograph of the system 2 hardware is shown in Fig. 22. A summary of the relevant hardware parameters is given in Table 7.

Table 7 – System 2 Summary of Hardware Parameters

Parameter	Value
Guide Rail Target Material	SS400
Current Saturation Magnitude	4 (A)
Upper Platform Target Material	Iron
Lower Platform Material	Aluminum
Distance Sensor Type	Laser
Coil Windings per HEM	720 turns
HEM Pole material	23ZH100
HEM Coil Turns	720
HEM Coil Material	Copper
HEM Magnetic Pole Area	10x21 (mm)
Total Levitated System Mass	6 (Kg)
Eccentric Load Mass	0.45 (Kg)
Eccentric Load Coordinates {x, y}	{0.25, 0.25} (m)

3. Experimental Procedure

The hardware calibration and experimental procedure for each of the conducted trials is described in this section. I should be noted that the placement of the eccentric mass is always conducted by hand, and the mass is always placed in the same location on the upper platform as is defined in Table 7. An overview of the conditions of the conducted trials is tabulated in Table 8 and a written description is given for each trial in its respective subsection.

Table 8 – Summary of Experimental Trails

	Trial Name	Tip-Tilt $\{\alpha, \theta\}$ (rad)	Eccentric Load	ZP Tip-Tilt Control	Angle Tracking
Trial 1	Horizontal Pre-Load	{0,0}	Before t=0	After t=0	Before t=0
Trial 2	Horizontal Post-Load	{0,0}	After t=0	Before t=0	Before t=0
Trial 3	Tilted Post-Tilt	{0,-0.15}	After t=0	Before t=0	After t=0
Trial 4	Tip-Tilted Pre-Tilt	{0.1,0.1}	After t=0	After t=0	Before t=0

A summary of the relevant parameters used in all trials is tabulated in Table 9.

Table 9 – System 2 Summary of Experimental Parameters

Trial Number	Parameter	Value
1	Displacement Controller Activation Timing	t=5(s)
1	Approximate Settling Time	30 (s)
2	Load Placement Timing	t=10(s)
2	Approximate Settling Time	30(s)
3	Step Tilt Target Timing	t=10(s)
3	Approximate Settling time	50(s)
4	Displacement Controller Activation Timing	t=10(s)
4	Approximate Settling Time	50(s)

3a. Calibration

For each experimental trial, the laser distance sensors are recalibrated such that they read zero distance when the HEMs are in contact with the magnetically permeable target. The starting zero positions of the permanent magnets in the displacement system is defined as the locations

where the system is able to achieve zero-power levitation when unloaded. To calibrate this starting position, the system is let to reach unloaded steady-state levitated equilibrium with the displacement controller activated. Once this is achieved, the location of the permanent magnets is recorded as the reference zero for the experimental trial. This calibration is conducted before the commencement of each trial.

3b. Horizontal Pre-Load Trial

For the horizontal pre-load trial, the system is first let to reach levitated steady-state with the air-gap controller tracking a zero tip-tilt and with the displacement controller deactivated. The eccentric weight is then placed by hand on the corner of the levitated platform, and the system is let to reach steady-state again before time t=0. After time t=0, after short period of steady-state stability, the displacement controller is activated and the permanent magnets are let to converge zero-power steady-state equilibrium before the experiment is ended. Specific details of this experimental trial are tabulated in Table 7 and Table 9.

3c. Horizontal Post-Load Trial

For the horizontal post-load trial, the system is first let to reach levitated stead-state with the air-gap controller tracking zero tip-tilt and with the displacement controller activated. After time t=0, after a short period of steady-state stability, the eccentric mass is placed on the corner of the levitated platform and the system is allowed reach its new zero-power steady state equilibrium before the trial is ended. Specific details of this experimental trial are tabulated in Table 7 and Table 9.

3d. Tilted Post-Tilt Trial

For the tilted post-tilt trial, the system is first let to reach levitated steady-state with the air-gap controller tracking a zero tip-tilt and with the displacement controller activated. The eccentric mass is then placed by hand on the corner of the levitated platform, and the system is let to reach steady-state again before time t=0. After time t=0, after a short period of steady-state stability, the tilt target of the system α_{Tar} is changed to 0.15 radians and the system is allowed to reach its new zero-power steady-state equilibrium before the experiment is ended. Specific details of this experimental trial are tabulated in Table 7 and Table 9.

3e. Tip-Tilted Pre-Tilt Trial

For the tip-tilted pre-tilt trial, the system is first let to reach levitated steady-state with the air-gap controller tracking a 0.1 radian tilt in both α_{Tar} and θ_{Tar} and with the displacement controller deactivated. The eccentric mass is then placed by hand on the corner of the levitated platform, and the system is let to reach steady-state again before time t=0. After time t=0, after a short period of steady-state stability, the displacement controller is activated and the system is allowed to reach its new zero-power steady-state equilibrium before the experiment is ended. Specific details of this experimental trial are tabulated in Table 7 and Table 9.

4. Experimental Data
4a. Controller Tuning and Data Processing

The starting controller gains for the levitation hardware were inherited from previous research [5] and were empirically adjusted to account for the additional loads caused by the integration of the displacement system.

The tip-tilt controller gains k_{Ix} and k_{Iy} are physically limited by the maximum velocity achievable by the stepper motors. Initially, the tip-tilt controller gains were set to zero and then were slowly increased until it was observed the maximum velocity of the stepper motor was met under normal operating conditions. From there, the gains were empirically reduced to minimize vibrations and improve performance. For simplicity, the controller gains in x and y were kept identical.

To remove unwanted vibrations and noise in the data and to more clearly show the steady-state and dynamic trends, the data presented in the following section is filtered using a running average filter with a window of one second. As the sampling frequency is 10 kilohertz, this is equivalent to averaging 10,000 samples.

4b. Horizontal Pre-Load Trial
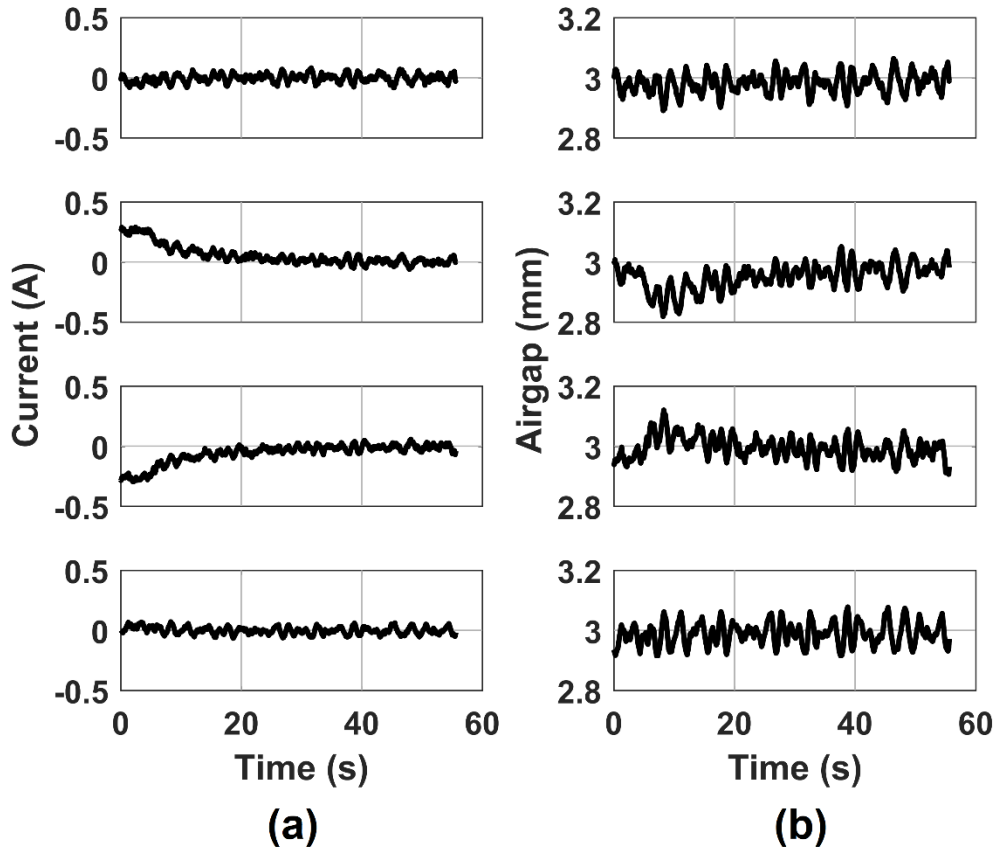
Fig. 23 – (a) Current and (b) air-gap data from the horizontal pre-load trial.

The current and air-gap data collected for the pre-load trial is shown in Fig. 23(a) and Fig. 23(b), respectively. In this trail, the levitation system was disabled initially and activated after roughly five seconds. The exact timing of activation can be more clearly seen in Fig. 24. From the current data in Fig. 23(a), it can be seen that the variance in currents before the tip-tilt controller was activated was steady-state and non-zero. After activation, it can be seen that all current channels converge to zero. Also, after activation, it can be seen in Fig. 23(b) that the air-gaps converge back to their original value after a short transient period.
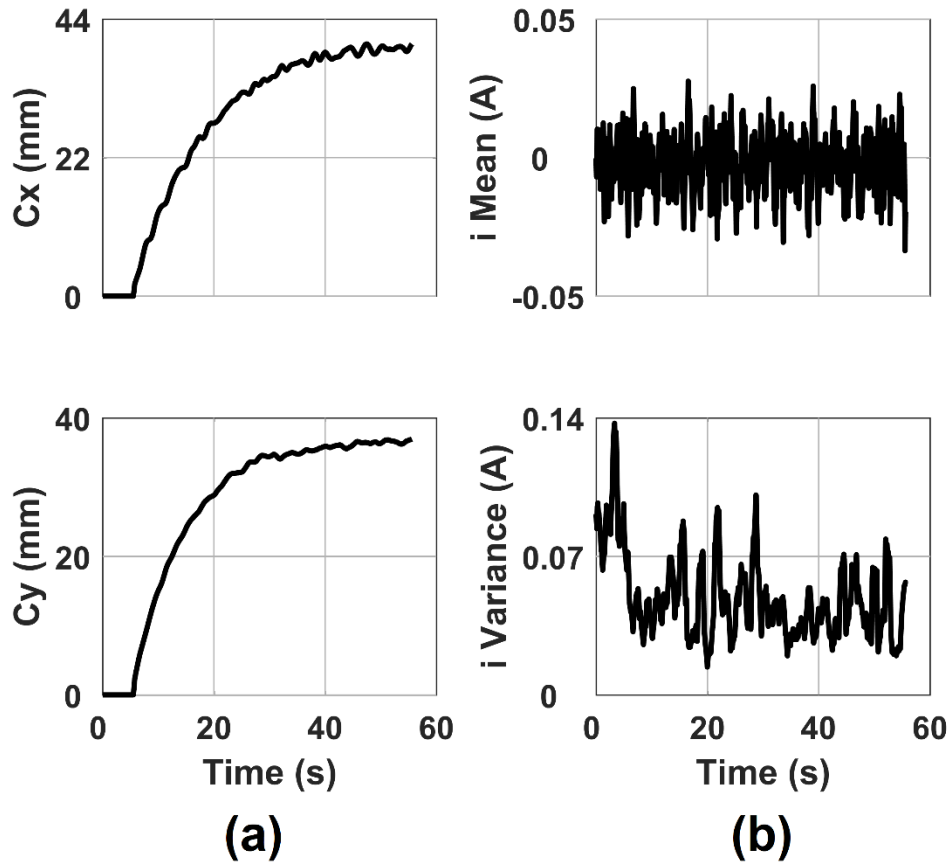
Fig. 24 – Permanent magnet location (a) and current metrics (b) for the horizontal pre-load trial.

The permanent magnet location data $\{C_x, C_y\}'$ and current metrics for the system for the horizontal pre-load trial are shown in Fig. 24(a) and Fig. 24(b) respectively. It can be seen in Fig. 24(a) that the velocity of neither C_x nor C_y reached saturation as no straight sections on the curve are present. It should be noted that in Fig. 24(b) that current variance does not converge to zero as variance is not a signed value and will not converge to zero if there is noise present in the data. For all four trials, it should be understood that as higher specification equipment is used and noise is reduced, variance in currents will also be reduced. In a theoretically ideal system, current variance would approach zero.

4c. Horizontal Post-Load Trial
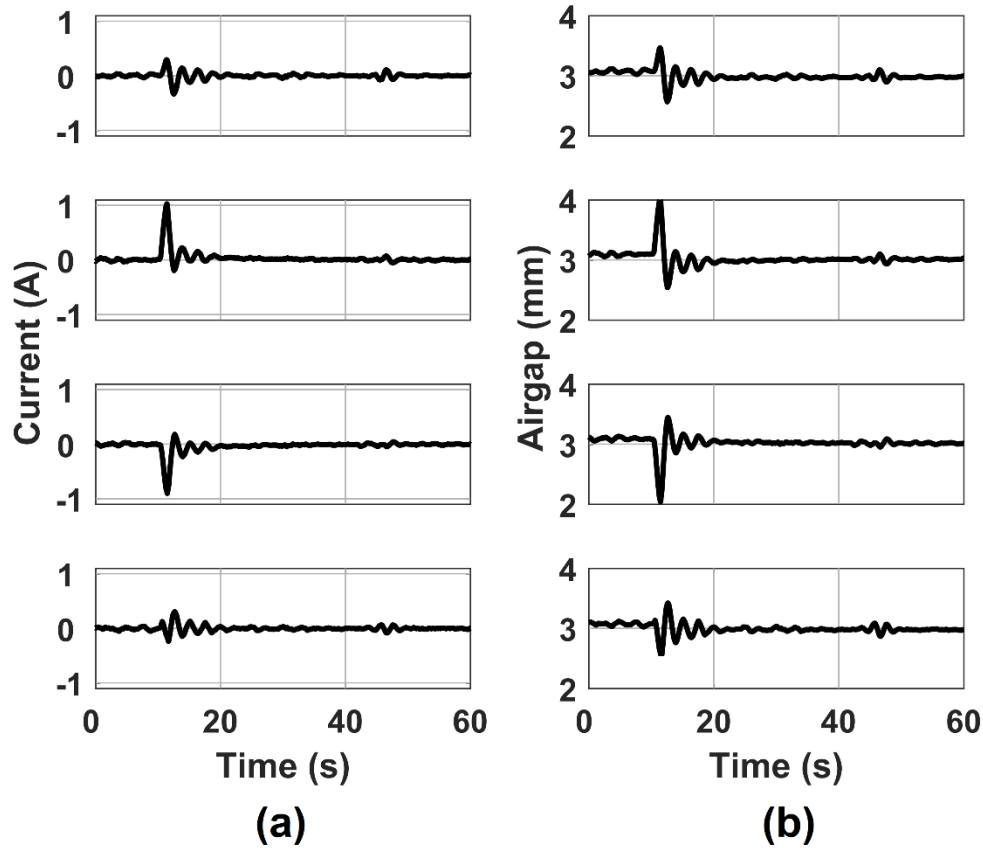
Fig. 25 – (a) Current and (b) air-gap data from the horizontal post-load trial.

The current and air-gap data collected for the post-load trial is shown in Fig. 25(a) and Fig. 25(b), respectively. In this trial, the tip-tilt controller was activated prior to placing the eccentric mass on the platform after roughly 10 seconds. There is a small oscillation visible at roughly 45 seconds which is expected to have been caused by contact between the levitated platform and an x-direction restraining guide. In Fig. 25(b), the zero-power air-gap is seen to have decreased after placing the eccentric mass. This phenomenon is expected due to the negative-stiffness characteristics of the zero power z-height feedback loop [1,4,6]. In Fig. 25(a) it is confirmed that zero-power is acheived both before and after placing the eccentric mass.
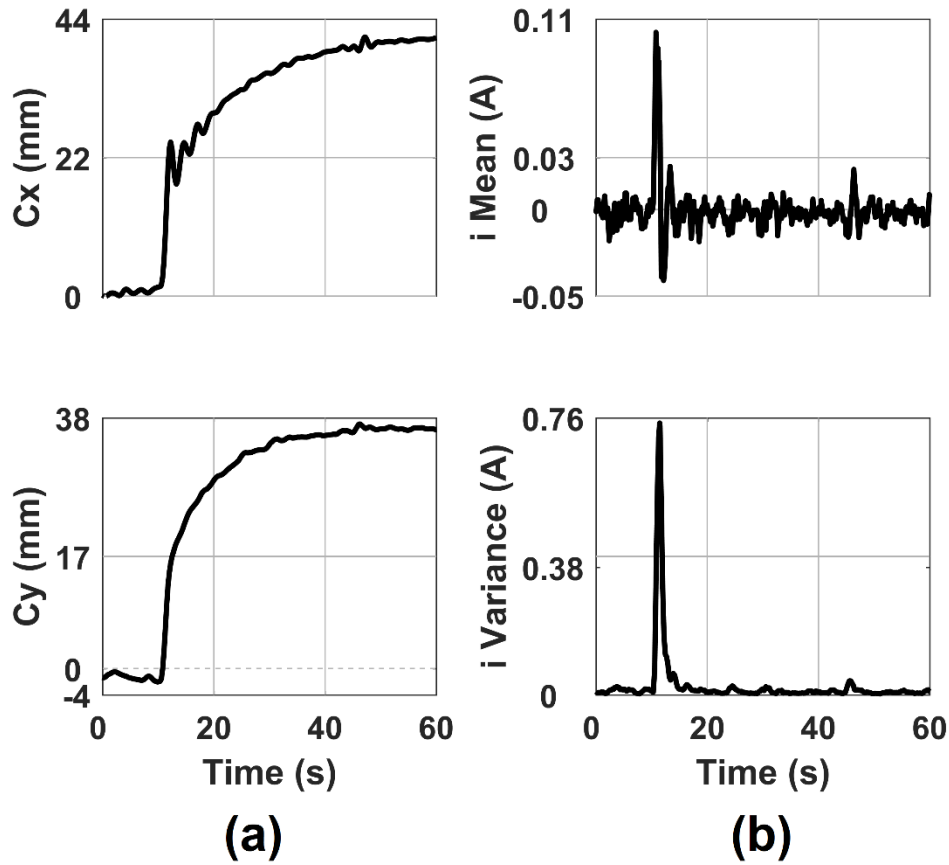
Fig. 26 – Permanent magnet location (a) and current metrics (b) for the horizontal post-load trial.

The permanent magnet location data $\{C_x, C_y\}'$ and current metrics for the system for the post-load trial are shown in Fig. 26(a) and Fig. 26(b) respectively. It can be seen in the C_x curve in Fig. 26(a) that velocity saturation for C_x occurred immediately after placing the mass on the platform. This is characterized by the straight portion of the curve, and it can be seen that small oscillations are caused immediately after result of integrator buildup and overshoot. The variance and mean current spikes in Fig. 26(b) can be seen to be larger than that of which was seen in the pre-load trial.

4d. Tilted Post-Tilt Trial
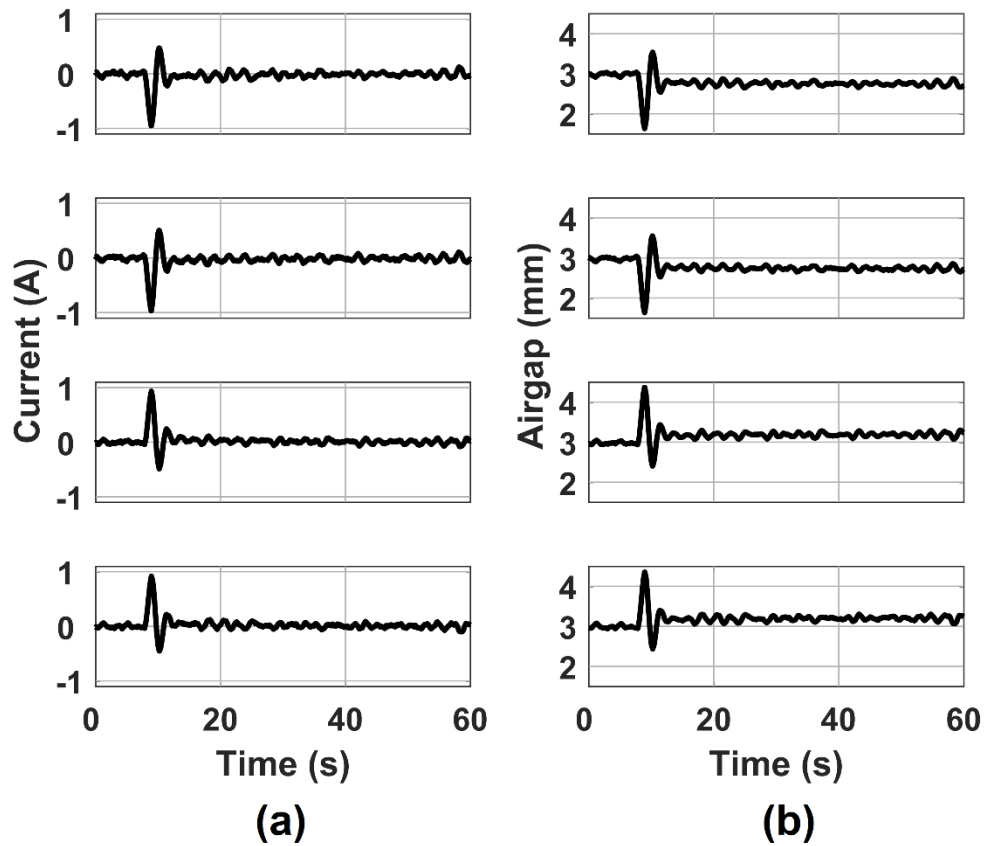
Fig. 27 – (a) Current and (b) air-gap data from the tilted post-tilt trial.

The current and air-gap data collected for the tilted post-tilt trial is shown in Fig. 27(a) and Fig. 27(b), respectively. In this trial, the system was let to reach steady-state unloaded horizontal equilibrium before a step-input tilt command was tracked by the air-gap controller after roughly 10 seconds. In Fig. 27(b) it can be seen that before the tilt command was tracked, the air-gap at each HEM was identical, corresponding to horizontal levitation. The steady air-gap data after the system was commanded to tilt is shown more clearly Fig 28.
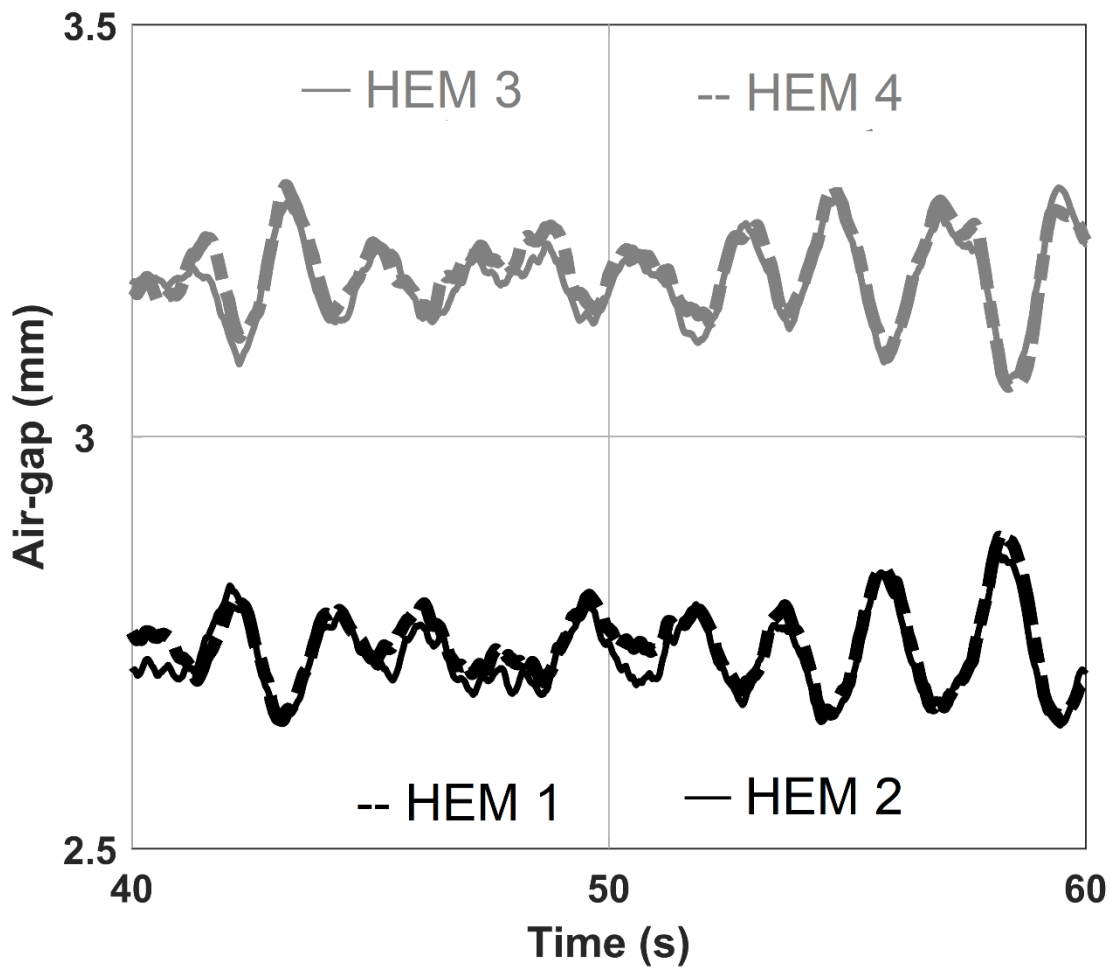
Fig. 28 – Zoomed current data for the tilted post-tilt trial.

In Fig. 28 it can be seen clearly that the air-gaps at HEM 1 and HEM 2 are nearly identical and that the air-gaps at HEM 3 and HEM 4 are nearly identical. This is representative of an angular tilt around the y-axis. Also, it can be seen that there is a strong similarity or symmetry between all four current channels. This phenomenon occurs because of the state-space controller used where the four current signals are created by a linear combination of three state variables. This similarity and symmetry is present in all experimental trials, but is more clearly seen when the data is enlarged.
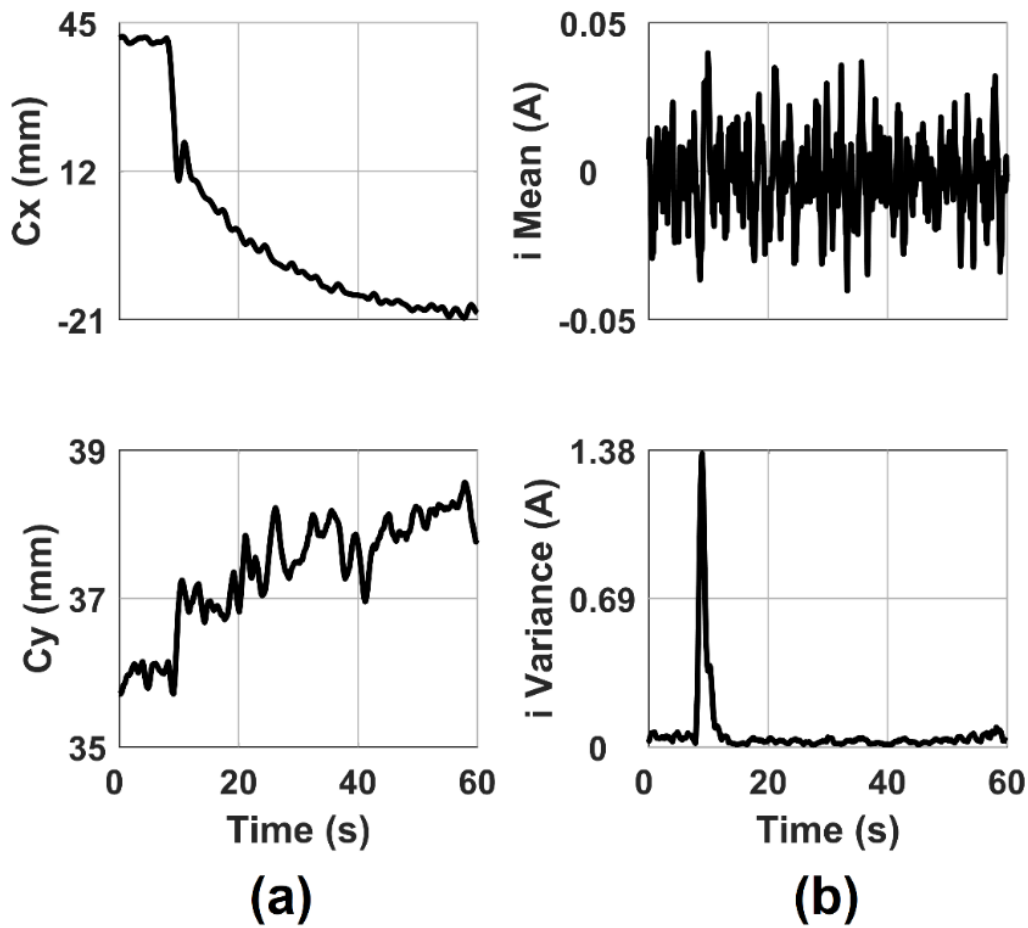
Fig. 29 – Permanent magnet location (a) and current metrics (b) for the tilted post-tilt trial.

The permanent magnet location data $\{C_x, C_y\}'$ and current metrics for the system for the tilted post-tilt trial are shown in Fig. 29(a) and Fig. 29(b) respectively. In this case, $\{C_x, C_y\}'$ do not start at zero because the system was let to reach zero-power equilibrium with an eccentric load before t=0. It can be seen in Fig. 29(a) that the overall displacement of C_x is greater than that of C_y. This result is explained as the rotation of the platform about the y-axes results in a much larger moment about the y-axis.

4e. Tip-Tilted Pre-Tilt Trial
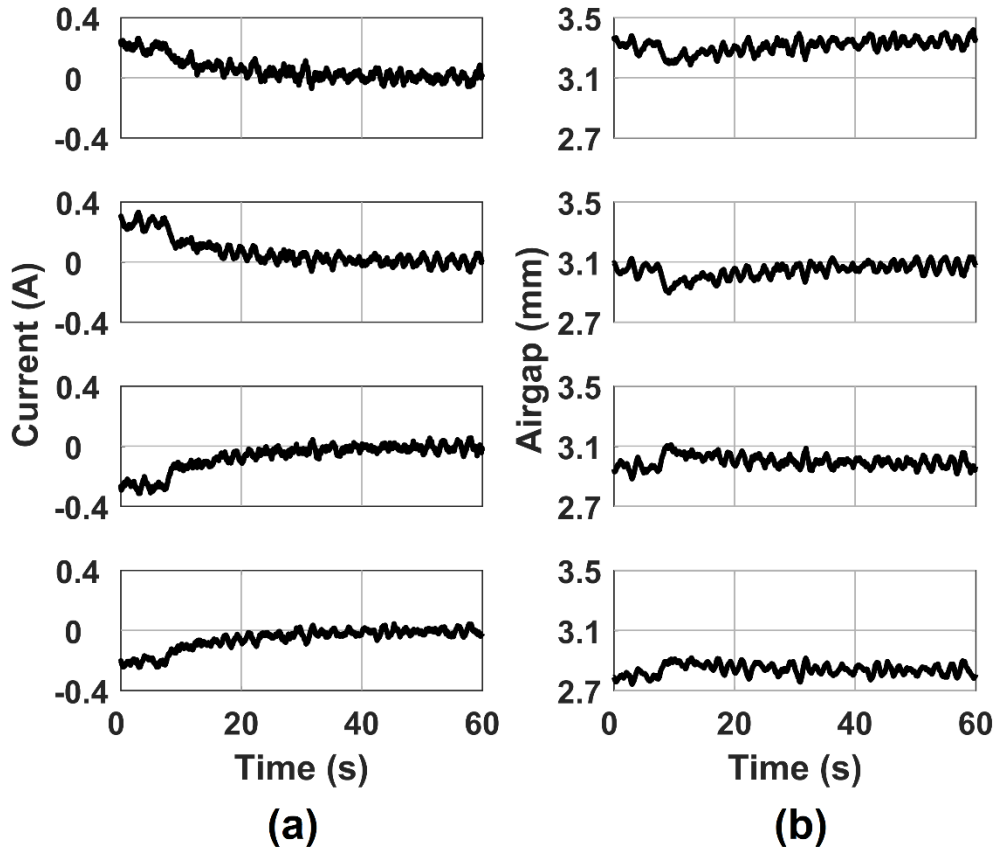
Fig. 30 – (a) Current and (b) air-gap data from the tip-tilted pre-tilt trial.

The current and air-gap data collected for the tip-tilted pre-tilt trial is shown in Fig. 30(a) and Fig. 30(b), respectively. In this trial, the system was let to reach steady state at an arbitrary tip-tilt before the zero power tip-tilt controller was activated. In Fig. 30(a) it can be clearly seen that initial current variance is non-zero, and converges to zero after the tip-tilt controller is activated. In Fig. 30(b) it can be seen that the air-gaps converge to their original values after the tip-tilt controller is activated, indicating good tracking performance. A zoomed view of the stead-state air-gap data is shown in Fig. 31.
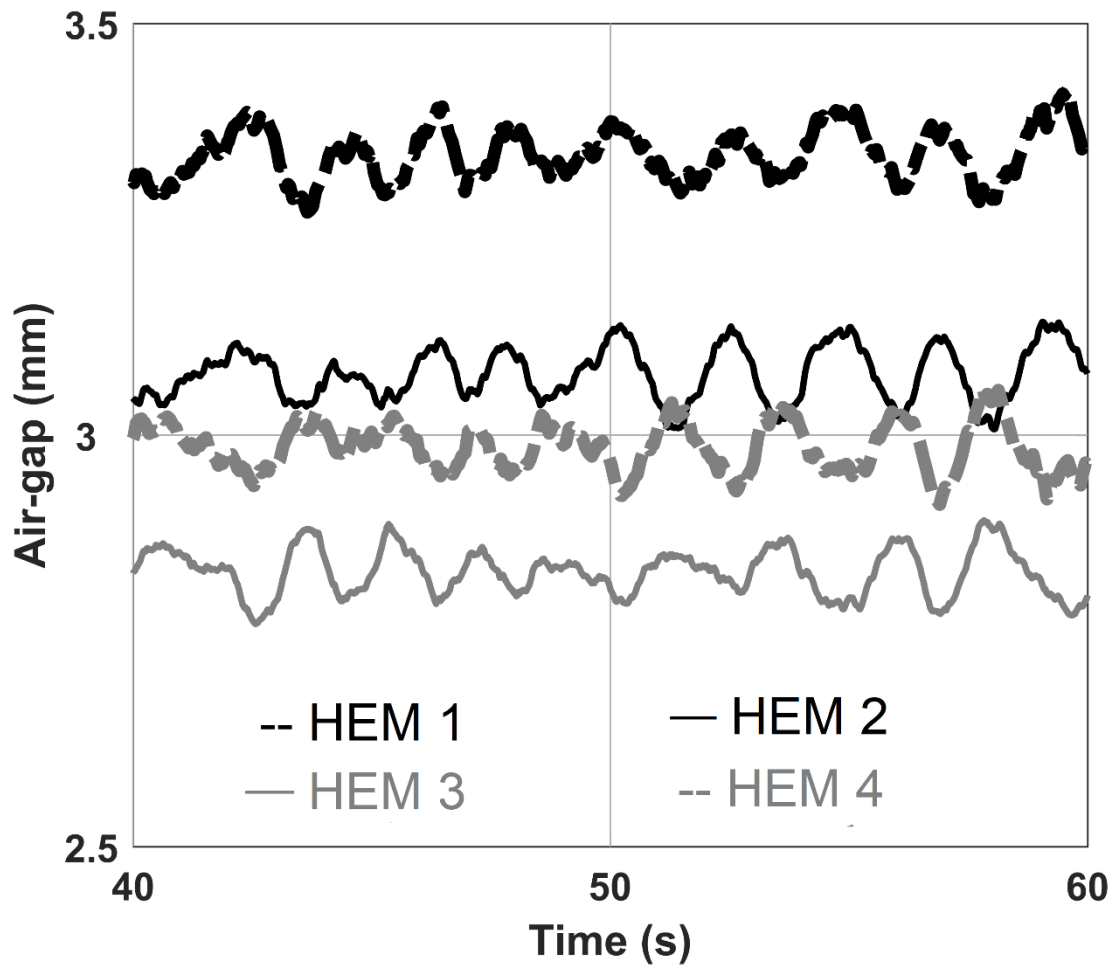
Fig. 31 – Zoomed current data for tip-tilted pre-tilt trial.

Again, in Fig. 31 the strong similarity and symmetry of the current channels can be observed. It can be see that all four channels are non-equal, indicating the system is successfully tracking an arbitrary tip-tilt.
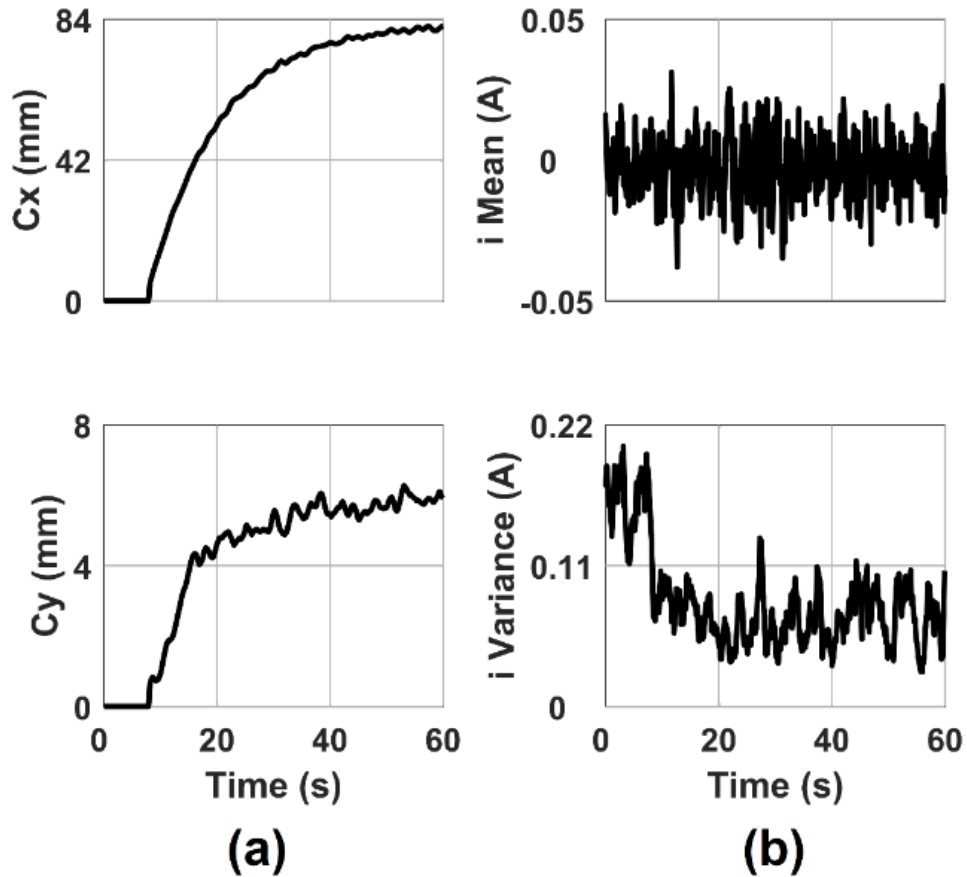
Fig. 32 – Permanent magnet location (a) and current metrics (b) for the tip-tilted pre-tilt trial.

The permanent magnet location data $\{C_x, C_y\}'$ and current metrics for the system for the tip-tilted pre-tilt trial are shown in Fig. 32(a) and Fig. 32(b) respectively. Again in Fig. 32(a), similar to the tilted post-tilt trial, a larger displacement is observed for C_x compared to C_y. In Fig. 32(b) it can be seen that current variance is reduced after the activation of the displacement controller. Compared with the horizontal pre-load trail in Fig. 24(b), the current variance in the tip-tilted pre-tilt trial in Fig. 32(b) is observed to be greater both before and after activating the tip-tilt controller. This can be attributed to the fact that lateral magnetic forces exist in the directions of the x and y axes when the system is not horizontal. As there is no active control for lateral forces, this is expected to result in greater levels of unwanted noise and vibration in the lateral directions.

Chapter 5 – Conclusion

1. System Comparison

Two experimental systems were developed to demonstrate zero-power tip-tilt controlled magnetic levitation under eccentric loading. System 1 was designed with the objective of examining the minimum system requirements necessary to achieve zero-power tip-tilt controlled levitation and system 2 was designed with objective of improving system performance.

It was found experimentally that compared to system 2, the stability of the system 1 was inferior. The unwanted vibrations in system 1 are primarily attributed to the use of a local control strategy where cross interference between local controllers at each HEM is expected. In system 2, a state-space controller was employed which controlled 4 HEM currents. As the command currents at each HEM were determined by a single state-space controller, local cross interface was not an issue and unwanted vibrations were greatly reduced.

The second largest contributor to unwanted vibrations in system 1 is posited to the uncontrolled lateral translations of the system. Again, this is slightly alleviated in system 2 by the design geometry of the HEMs and the passive magnetic rails [5].

Another distinct advantage of system 2 is the non-reliance of the displacement controller tuning on a non-linear transform. Because of this characteristic, the controller can be easily tuned by slowly increasing two integrator gains, and further no hardware calibration is required.

When comparing the economics of system 1 and system 2, system 1 has a clear advantage as only 3 HEMs, 3 current amplifiers, ands 3 laser distance sensors are required. System 2 employs 4 HEMs, 4 current amplifies, and 4 laser distance sensors.

2. Summary

In summary, a method to achieve zero-power tip-tilt controlled magnetic levitation under eccentric loading was proposed. The basic principle behind the control strategy was explained, and two systems were designed, produced, and tested to verify the validity of the control strategy.

System 1 successfully demonstrated experimentally and through simulations that zero-power horizontal levitation under eccentric loading was possible with 1 fixed HEM and 2 moving

HEMs. System 2 successfully demonstrated experimentally that zero-power tip-tilt orientation control under eccentric loading was possible with active tip-tilt tracking.

To the extent of background research conducted, no other systems have demonstrated zero-power tip-tilt control under eccentric loading. It is anticipated that this control methodology can be applied to many already existing magnetic levitation systems.

3. Suggestions for Future Work
3a. Novel Moving Magnet Configuration for Linear Sliders
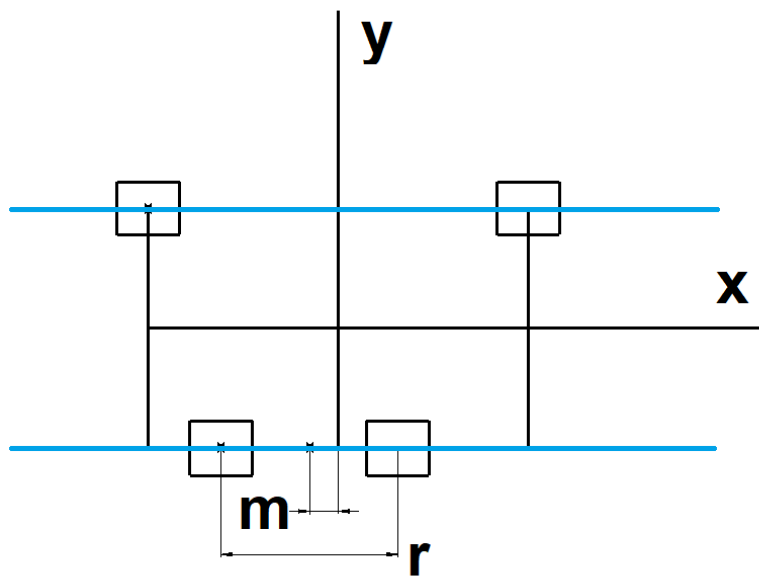
Fig. 33 – Schematic of the proposed HEM displacement strategy where the location of magnetically permeable rails are indicated in blue.

System 2 was integrated into a linear slider, however an additional iron plate was required between the two originally existing magnetically permeable rails as one permanent magnet pair was allowed to move in the x direction and the other pair was allowed to move in the y direction. In the case of a linear slider, it would be greatly beneficial if the HEMs were only required to move in a single direction. In such as case, an additional iron plate would not be required between the magnetically permeable rails. It can be seen in Fig. 33 that if the bottom pair of HEMs were allowed to move only in the x direction, they would always be aligned with the rail used by the slider itself indicated in blue. It can be easily understood that moving the median point *m* between the two lower HEMs in the x direction can create moments about the y-axis. Here, it is further

proposed that the novel HEM configuration shown in Fig. 35(a) can also allow moments the be created about x-axis by adjusting the distance *r* between the two HEMs. A first order analysis is described below to characterize the separation-moment relationship.
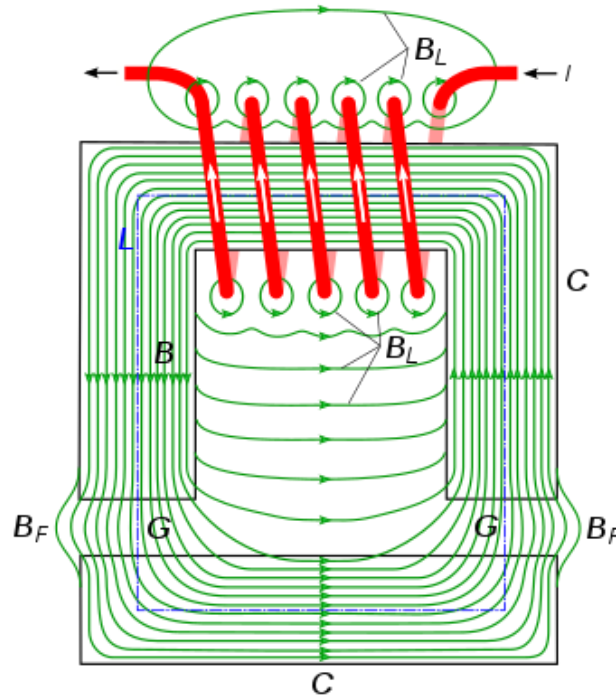
Fig. 34 – Example of an electromagnetic circuit. For a HEM, a permanent magnet is inserted with the north-south poles in the direction of magnetic flux.

In an electromagnetic circuit such as the one shown in Fig. 34, the virtual work method can be used to calculate the attractive magnetic force

$$F = \frac{\delta W}{\delta L} \tag{45}$$

where δL is the air-gap and where

$$\delta W = \frac{1}{2}\int_0^v \frac{B^2}{\mu_0} dv. \tag{46}$$

Solving (45) and substituting into (46) yields the relationship

$$F = \frac{B^2 A}{2\mu_0} = \frac{\phi^2}{2A\mu_0} = K\phi^2 \tag{47}$$

From (47) it can be seen that force is proportional to the square of total flux through the circuit.
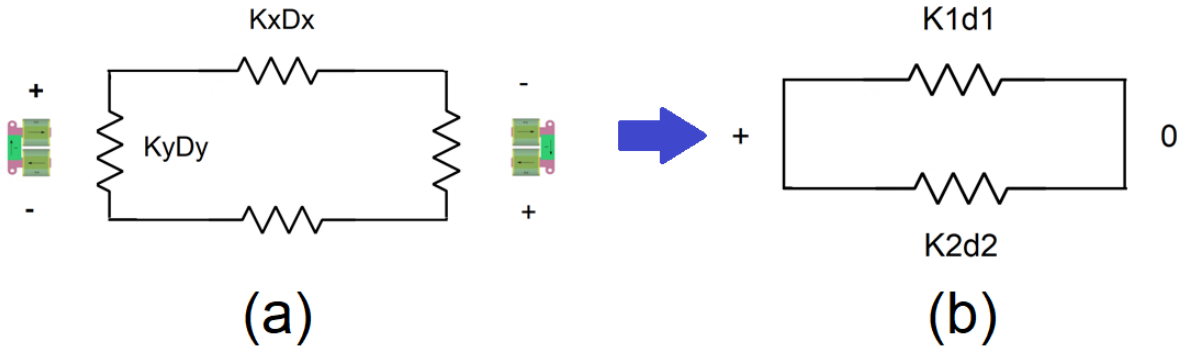
Fig. 35 – (a) Equivalent circuit for the system shown in (37). (b) An mathematically simplified but equivalent circuit.

Consider then the electromagnetic circuit depicted in Fig. 35(a) which can be simplified to the circuit in Fig. 35(b) due to symmetry. These equivalent circuits are representative of the interactions which can be expected form the system depicted in Fig. 37. In these circuits, an analogy between an electromagnetic circuits and electrical circuits is used relating (48) and (49)

$$V = IR \tag{48}$$

$$MMF = \phi * R_E, \tag{49}$$

where MMF is the magnetomotive force, ϕ is magnetic flux, and R_E is magnetic reluctance. For the circuit in Fig. 35(b), the magnetic reluctance can be varied by increasing the distance between the HEMs d_1 as described by

$$R_{EQ} = \frac{R_1 R_2}{R_1 + R_2} = \frac{d_1 k_1 d_2 k_2}{d_1 k_1 + d_2 k_2}. \tag{50}$$

where, k_1 and k_2 are the magnetic reluctances per unit length of the material in the d_1 and d_1 directions respectively. It is known that laminated composites such as the one depicted in Fig. 37 are able to have magnetic reluctances which differ depending on direction.

Next, the relationship between flux and resistance can then be rewritten as

$$\frac{\phi}{MMF} = \frac{1}{R_E} = \frac{d_1 k_1 + d_2 k_2}{d_1 k_1 d_2 k_2} \tag{51}$$

which can be reorganized into

$$\frac{d_2 k_2}{MMF} \phi = \frac{\left(\frac{d_1 k_1}{d_2 k_2}\right) + 1}{\left(\frac{d_1 k_1}{d_2 k_2}\right)}. \tag{52}$$

If we define two new variables x and y such that

$$x \triangleq \left(\frac{d_1}{d_2}\right)\left(\frac{k_1}{k_2}\right) \qquad (53)$$

$$y \triangleq \frac{d_2 k_2}{EMF} \phi \qquad (54)$$

(52) can be reduced to

$$y = \frac{x+1}{x}. \qquad (55)$$
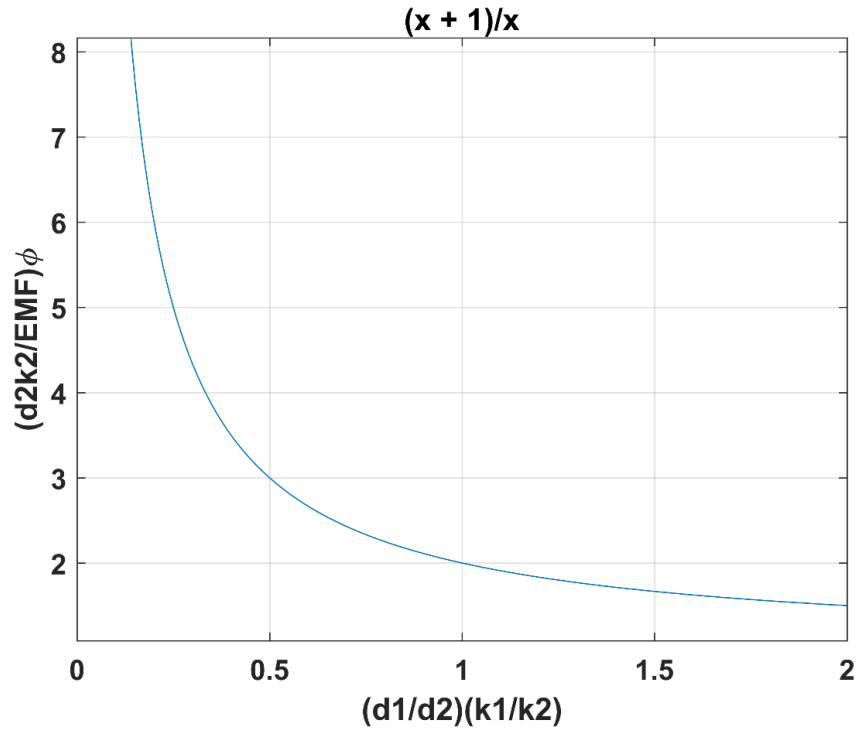
Fig. 36 – Graphical depiction of (55).

      The solution to (55) is depicted in Fig. 36. Using this figure, it can be understood that the sensitivity of flux ϕ change to change in distance d_1 between the two HEMs increases as k_1/k_2 decreases. With this understanding, the laminated rail oriented as shown in Fig. 37 can be designed, where higher resistance is desired in the direction of d_2.
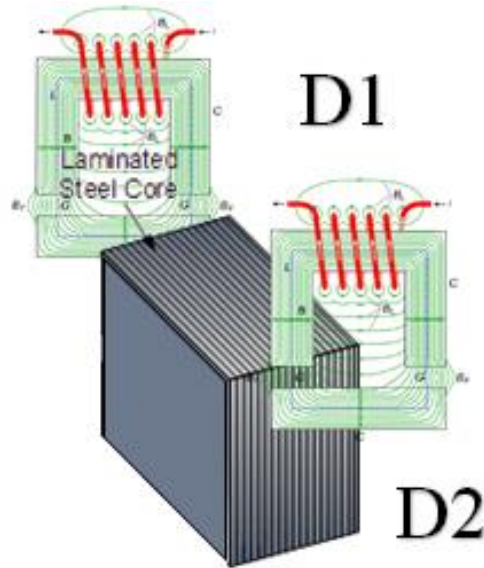
Fig. 37 – Schematic drawing showing the proper orientation of laminations where D2 is the distance between the cores of a single hem and D1 is the distance between the 2 HEMs.

It is given here that the magnetic permeability of iron is roughly 5000 times that of air, where magnetic reluctance is given by the relationship

$$R_n = \frac{l_n}{\mu_n A_n} . \tag{56}$$

Then, if a laminated material is created with 20% of the volume being air, the ratio of the reluctance of the laminated material in the direction perpendicular to the air-gaps, compared to the reluctance of solid iron is given by

$$\frac{R_{Lam}}{R_{Iron}} = \frac{\mu_{Iron}}{\mu_{Lam}} = 5000 \left(\frac{0.8}{5000} + \frac{0.2}{1} \right) = 500.9 \tag{57}$$

It then follows that

$$\frac{k_1}{k_2} = \frac{1}{500.9}. \tag{58}$$

If we assume that

$$5 < \frac{d_1}{d_2} < 15 \tag{59}$$

meaning that the range of motion between the two HEMs is 5 to 15 times the distance between the poles in a single HEM, it can be calculated that

53

$$\frac{\frac{15}{500.9}+1}{\frac{15}{500.9}} < \frac{d_2 k_2}{EMF}\phi < \frac{\frac{5}{500.9}+1}{\frac{5}{500.9}} \tag{60}$$

$$34.9 < \frac{d_2 k_2}{EMF}\phi < 102.8 \tag{61}$$

$$\frac{d_2 k_2}{EMF}\phi = 67.9 \pm 49\%. \tag{62}$$

It can be interpreted form (62) that a flux change of 49% in either direction from the mean flux can be achieved by moving the HEM as described in the parameterization as long as magnetic saturation does not occur.

Recalling (47), it can be understood that the change in force is always increases with increases in flux since the derivative of (47) is monotonic

$$F' = 2K\phi. \tag{63}$$

It can then be concluded that resulting from the flux range described in (62), an even greater range will result in force which can then be used to produce moments about the x axis.

$$F_{range} = F_{mean} \pm (> 49\%). \tag{64}$$

It should be noted that this analysis is only conducted as a starting point for future research. It is expected that non-linearity will occur in the physical realization of the system due to flux losses and to magnetic saturation. However, the results in (64) strongly support the viability of this strategy, and the analysis has given a starting point on how to design the laminated rails and HEMs.

3b. System 1 State Space Control

Future researchers who will conduct research on zero-power magnetic levitation at the Kochi University of Technology in Oka-Harada Lab will have access to the hardware and control software developed for system 1 and system 2 presented in this dissertation. As a starting point for these future researchers, it is suggested that a state-state space controller similar to the one that is employed in system 2 is developed for system 1. In the current state of the hardware, it is believed that the upgrade to state-space control will be the largest contributor in reducing unwanted vibrations in system 1. It is anticipated that the largest difficulty in developing a state-space controller for system 1 will be gain scheduling because the HEMs continuously move. As a starting point, it is recommended that a LPV system first be described for system 1 in state-space. From

there, tuning can be conducted for individual systems and eventually a smooth linear interpolation can be achieved.

Appendix

1. Existence of Arbitrarily Close Equilibrium Orientations

1a. Introduction

It was shown in this dissertation that zero-power magnetic levitation can be achieved by maintaining a magnetically levitated platform in an equilibrium tip-tilt orientation. However, it was considered that an issue in control could occur if more than one equilibrium orientation existed for a given force-moment load.

This issue would be further amplified if multiple equilibrium orientations were to be so similar that the difference could not be distinguished by the resolution of the distance sensors. In such as case, the controller would be prone switching the systems orientation between the two arbitrarily close equilibrium orientations.

To answer the question of whether multiple equilibrium positions exist for a given load and to describe the conditions of arbitrarily close multiple equilibrium positions, a mathematical analysis is in two dimensions is conducted [21].

1b. Mathematical Formulation

Fig. 38 – Schematic drawing used for analysis of multiple equilibrium.

A schematic drawing of a generalized 2 DOF, 2 magnets, symmetric, maglev platform is shown in Fig. 38 where

z_n^* is the effective distance of point 'n'

F_{EQ} is the equivalent force load

M_{EQ} is the equivalent moment load

$F_{M,n}$ is the magnetic force at point 'n'

L is the length of platform

θ is the tilt angle of the platform.

Geometrically, it can be developed that

$$z_1^* = z_0^* + \frac{L}{2}\sin\theta \tag{65}$$

$$z_2^* = z_0^* - \frac{L}{2}\sin\theta. \tag{66}$$

It can be seen that z_0^* and θ fully define the orientation of the platform. The force profile at each magnet location can be described as

$$F_{M,n} = \frac{K}{z_n^{*2}}. \tag{67}$$

Next, equations of static equilibrium are established and two new variables K_F and K_M are defined in (68) and (69) respectively. The inverse proportionality of K_F and K_M is used to simplify analysis.

$$F_{EQ} = \frac{K}{K_F} = F_{M,1} + F_{M,2} \tag{68}$$

$$M_{EQ} = \frac{K}{K_M} = \frac{L}{2}\cos\theta(F_{M,1} - F_{M,2}) \tag{69}$$

By substituting variables and simplifying, (68) can be expressed in the biquadratic form

$$z_0^{*4} + Az_0^{*2} + B = 0 \tag{70}$$

where

$$A = -2K_1 - \frac{1}{2}L^2\sin^2\theta, \quad B = \frac{1}{16}L^4\sin^4\theta - \frac{1}{2}K_1L^2\sin^2\theta. \tag{71}$$

The solution to (70) has 4 roots, however Considering z_n^* must be greater than zero for all n, (72) becomes the only valid solution.

$$z_0^* = \left(\frac{1}{2}((A^2 - 4B^2)^{\frac{1}{2}} - A)\right)^{\frac{1}{2}} \tag{72}$$

(72) can be expanded as

$$z_0^* = \left(K_F + \left(K_F (L^2 \sin^2 \theta + K_F) \right)^{\frac{1}{2}} + \left(\frac{L^2 \sin^2 \theta}{4} \right)^{\frac{1}{2}} \right)^{\frac{1}{2}}.$$

(73)

Further, (69) can be expanded as

$$\frac{K_M L}{2} \cos \theta \left(\frac{1}{\left(z_0^* + \frac{L}{2} \sin \theta \right)^2} - \frac{1}{\left(z_0^* - \frac{L}{2} \sin \theta \right)^2} \right) = 1.$$

(74)

(68) and (69) represent the two necessary and sufficient constraints required for static equilibrium. Substituting (68) into (69) yields the single necessary and sufficient equation which represents all possible equilibrium spaces

$$(2G_A + \mathrm{L}\sin\theta)^2 (2G_A - 16L\sin\theta)^2 G_B) G_A = 0$$

(75)

where

$$G_A = \left(K_F + \left(K_F (L^2 \sin^2 \theta + K_F) \right)^{\frac{1}{2}} + \frac{L^2 \sin^2 \theta}{4} \right)^{\frac{1}{2}}$$

(76)

$$G_B = K_M L^2 \cos \theta \sin \theta .$$

(77)

If we define a new unit of length C_L which is equivalent to the length of the platform, and scale all other lengths to C_L, we may set $L=1$ in (75). After doing so, (75) becomes an equation of 3 variables: K_F, K_M, and θ. The solution to (75) is shown in Fig. 39.
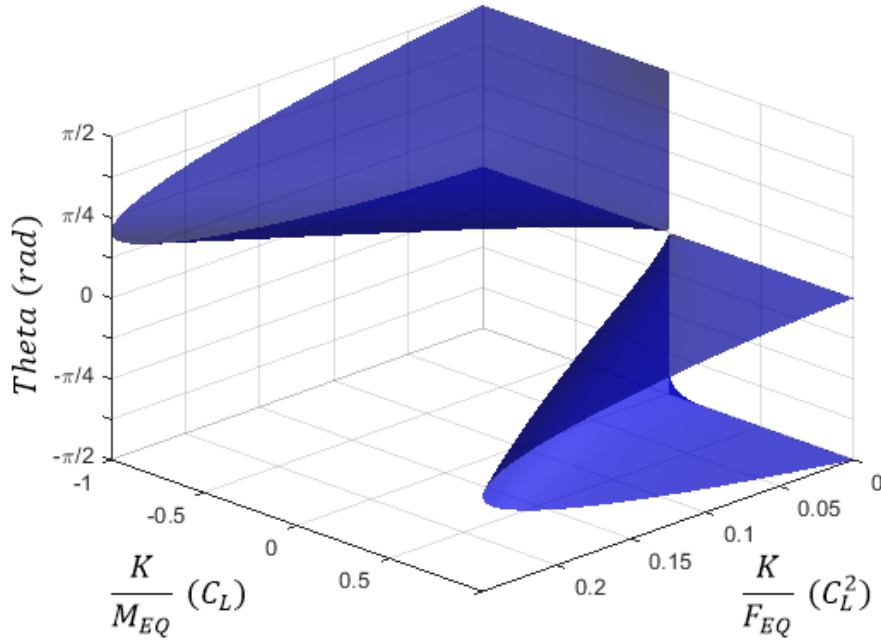
Fig. 39 – Graphical solution for (74).

When examining the axes of Fig. 39 the axes will be referred to force and moment axes. As the solution to (75) is symmetric about the force axis, only solutions in the positive force, positive moment octant will be discussed.

1c. Solution Interpretation

The surface depicted in Fig. 39 can be used to graphically determine the values of θ which are required for static equilibrium given applied loads F_{EQ}, M_{EQ} and the force constant K. θ can then be used to determine z_0^* using (73). To use Fig. 38, given values for F_{EQ}, M_{EQ}, and K are used to determine the operating point on the force-moment plane. Next, a vertical line passing through this point is drawn and the intersections between this line and the solution surface represents the θ values which correspond to equilibrium. If the line does not interest the surface, the given force-moment pair is not achievable in a zero-power system.

Arbitrarily close solutions exist when the vertical line is tangent to the solution surface as a small change in the operation point would cause a single intersection to bifurcate into a double intersection. The location of arbitrarily close equilibrium orientation is shown in a 2 dimensional graph in Fig. 40.
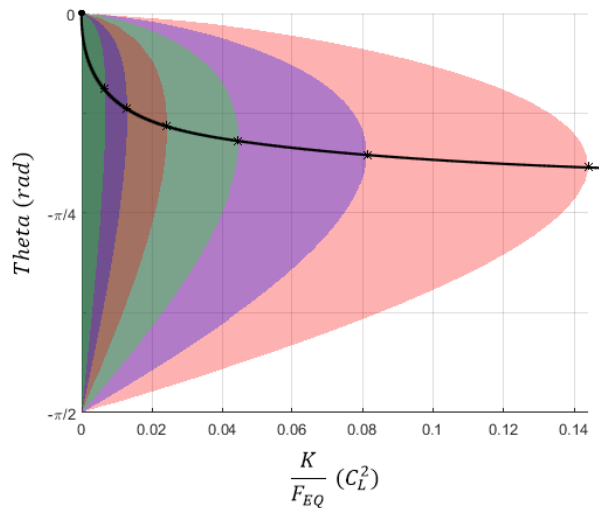
Fig. 40. 2D solution representation. Boundaries from right to left represent constant of slices $K_M = 0.5^X$ for x=1, 2, 3, 4, 5, 6

Fig. 39 is depicted by filled regions with alternating colors to emphasize that a solution *surface* is being shown where the boundaries between different colors represent slices where K_M is constant. The boundaries from right to left represent $K_M = 0.5^X$ for x=1, 2, 3, 4, 5, 6. If a vertical line representing an operating condition of the system were to be moved from right to left in Fig. 40, the points of intersection

between the line and the boundary would be arbitrarily close along the black curve indicated Fig. 40. As the black curve approaches the origin on the left, this indicates that it is possible for arbitrarily close equilibrium orientations to exist even at low angular tilts.

1d. Numerical Examples

It is important to verify that the interpretations made are physically relevant, meaning that the solutions are feasibly achievable without requiring unachievable conditions such as infinite or zero loads or distances. To this goal, numerical examples will be presented with cart parameters taken from the system 2 from the dissertation. The relevant parameters are tabulated in Table 10.

Table 10 – Multiple Equilibrium Parameters

Parameter	Description	Value
L	Cart Length	0.22 m
K	Defined in Eq.3	2*4.0982e-4 Nm²
m	System Mass	5.1 Kg
T	Operating Torque	0.5 Nm
c	Reference Height	1.3 mm

For this system, consider a total force load F_{EQ} of 100N, which is approximately equivalent to the weight of the system unloaded system. Considering the previously made interpretations, arbitrarily close equilibrium will exist near the limit of the highest moment achievable for a given force. Further, it is known zero power can only be achieved when the center of mass of the system and its load rests between the two magnets. With this knowledge, it can be inferred that the moment load M_{EQ} which will result in arbitrarily close equilibrium should be approximately equivalent to

$$M_{EQ} \approx \frac{L}{2}F_{EQ} \tag{78}$$

With this as a starting point, a numerical search can be conducted to find solution to M_{EQ} of 10.736 Nm. The complete solution is tabulated below:

Table 11 – Multiple Equilibrium Numeric Solution 1

Parameter	Description	Value
F_{EQ}	Equivalent Force Load	100 N
M_{EQ}	Equivalent Moment Load	10.737 Nm
$\theta,1$	First Solution Angle	-0.1530 rad
$z_0^*,1$	First Solution Height	0.0196 m
$\theta,2$	Second Solution Angle	-0.1505 rad
$z_0^*,2$	Second Solution Height	0.0194 m

It can be seen that final the numeric solutions for the equilibrium tilts θ in Table 11 differ by less than 2 percent.

By intentionally adjusting the parameters, the equilibrium tilts can be moved further away from one another as is a characteristic of being arbitrarily close. Another solution is tabulated below which demonstrates this. In this situation the θ solutions differ by approximately 4 percent.

Table 12 – Multiple Equilibrium Numeric Solution 2

Parameter	Description	Value
F_{EQ}	Equivalent Force Load	100 N
M_{EQ}	Equivalent Moment Load	10.700 Nm
$\theta,1$	First Solution Angle	-0.1995 rad
$z_0^*,1$	First Solution Height	0.0247 m
$\theta,2$	Second Solution Angle	-0.1146 rad
$z_0^*,2$	Second Solution Height	0.0155 m

Through these two numeric examples, it can be seen that arbitrarily close equilibrium orientations can exist in a physically achievable system. Further the locations and conditions of existence of arbitrarily close equilibrium orientations can be clearly understood by interpretation of Fig. 39 and Fig. 40. Although the existence of arbitrarily close equilibrium orientations has mathematically been shown to exist, performance degradation due to their existence has not been observed in the experimental trials conducted the systems presented in this dissertation. This is because as described by (78) arbitrarily close equilibrium orientations exist only in highly eccentric loading cases where the center of mass of the system is near an outer edge of the platform.

2. Considered Alternatives

A number of alternative methods to achieve zero-power tip-tilt control under eccentric loading were considered before it was decided that lateral displacement of permanent magnets was the best solution. A couple alternatives are presented in this section.

2a. Flux Path Control
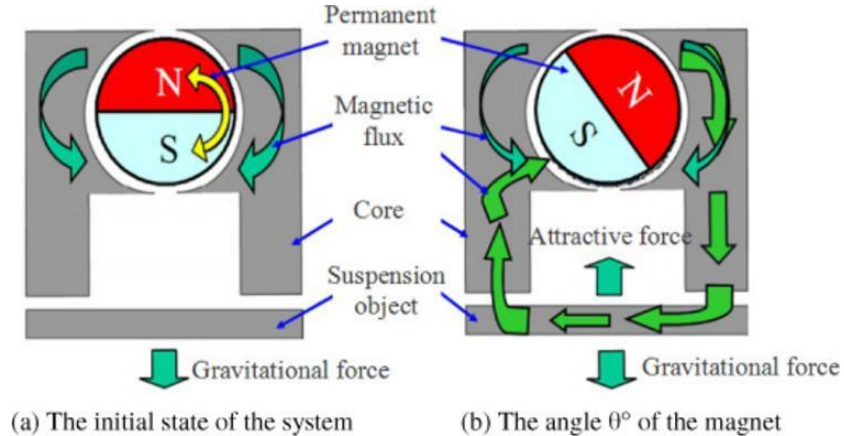
Fig. 41. Schematic diagram of one method of flux-path control. As the north south axis of the permanent magnet approaches the horizontal orientation, the magnetic flux, and thereof the attractive magnetic force approaches its maximum value. However, as the north-south axis moves away from the vertical orientation, a torque is induced, which requires active power. In the case of mechanical fixturing, continuous control cannot be achieved [22].

Flux path control is a control method which allows for the magnetic flux to be adjusted [22-23]. One flux-gate configuration which was previously researched at the Kochi University of Technology is shown in Fig. 41 [22]. This configuration allows magnetic flux to be altered by rotating a permanent magnet between two magnetically permeable pole pieces. It can be seen in Fig. 41(a) that symmetry allows for 0 magnetic flux to pass through the levitated portion while in Fig. 41(b) an asymmetry induces a magnetic flux.

It was considered that a flux adjustable passive magnetic force system could allow for a levitation system to account for eccentricities in loads, however to the extent of background research conducted, there are no flux-path control methodologies which allow for flux-gates to be held open without the need for an external holding force or torque. Because of this it was decided that the lateral displacement of permanent magnets would be a better solution as the displacement strategy does not rely on a holding force.

A levitation system which uses flux-path control is current being developed [24], however from discussion with the researcher, there not yet a plan to implement zero-power tip-tilt control at this time.

2b. Center of Mass Balance

Perhaps the most fundamental method of achieving zero-power tip-tilt control of magnetically levitated platforms is by using center of mass balance. In such a paradigm, if an eccentric load were placed on the levitated platform, another load could be placed to eliminate the eccentricity. For example, if a weight were added to the left of the platform, another weight on the platform could be moved to the right.

Mathematically, center of mass balance functions almost identically to the displacement of permanent magnets when a system is levitated horizontally. In the case of center of mass balance, a downward force is applied at the location of the mass, and in the case of moving permanent magnets, an upwards force is applied at the location of the centroid of the magnets. Ultimately however, since center of mass balance is not a topic which is unique to magnetic levitation, it was decided not to pursue this solution.

Bibliography

[1]   M. Morishita, T. Azukizawa, "Zero power control of electromagnetic levitation system", *Elect. Eng. Jpn.*, vol. 108, no. 3, pp. 111-120, 1988.

[2]   D. L. Trumper, T. Sato, "A vibration isolation platform", *Mechatronics*, vol. 12, pp. 281-294, 2002.

[3]   M. E. Hoque, M. Takasaki, Y. Ishino, and T. Mizuno, "Development of a three-axis active vibration isolator using zero-power control," *IEEE/ASME Trans. Mechatronics*, vol. 11, no. 4, pp. 462–470, Aug. 2006.

[4]   E. van West, A. Yamamoto, and T. Higuchi, "The concept of haptic tweezer, a non-contact object handling system using levitation techniques and haptics," *Mechatronics*, vol. 17, no. 7, pp. 345–56, Sep. 2007.

[5]   F. Sun, J. Jin, and K. Oka, "Noncontact Magnetic Suspension of an Iron Ball Using Flux Path Control Mechanism", *Advanced Materials Research*, vols. 230-232, pp. 573–577, 2011.

[6]   T. Mizuno, Y. Hirai, Y. Ishino, and M. Takasaki, "Flux-Path Control Magnetic Suspension System Using Voice Coil Motors", *Journal of System Design and Dynamics*, vol. 1(2), pp.147-158, 2007.

[7]   B. I. Annasiwaththa, K. Oka, "Design concept and analysis of a magnetically levitated linear slider with non-contact power transfer", *International Journal of Applied Electromagnetics and Mechanics*, vol. 52(1-2), pp. 207-213, 2016.

[8]   M. Morishita, T. Azukizawa, S. Kanda, N. Tamura, and T. Yokoyama, "A new maglev system for magnetically levitated carrier system," *IEEE Transactions on Vehicular Technology,* vol. 38, no. 4, pp. 230-236, Nov 1989.

[9]   H. Kim, J. M. Lee, H. S. Han, and B. S. Kim, "Levitation and thrust control of a maglev lcd glass conveyor," in *IECON* 2011 - 37th Annual Conference on IEEE Industrial Electronics Society, Nov 2011, pp. 610-615.

[10]   K. Kim, J. Han, C. Kim, J. Lee, and H. Han, "Dynamic analysis of maglev conveyor using an em-pm hybrid suspension," in *2011 IEEE International Conference on Mechatronics and Automation*, Aug 2011, pp. 2027-2032

[11]   C. H. Kim, K. J. Kim, J. S. Yu, and H. W. Cho, "Dynamic performance evaluation of 5-dof magnetic levitation and guidance device by using equivalent magnetic circuit model," *IEEE Transactions on Magnetics*, vol. 49, no. 7, pp. 4156-4159, July 2013.

[12]   Y. Ishino, M. Takasaki, and T. Mizuno, "Fabrication of non-contact carrier system using solar magnetic suspension*," Mechanical Engineering Journal Japan society of Mechanical Engineers*, vol. 2, no. 4, 2015.

[13]   T. Azukizawa, M. Morishita, S. Kanda, N. Tamura, and T. Yokoyama, "A linear induction motor control system for magnetically levitated carrier system," *IEEE Transactions on Vehicular Technology*, vol. 38, no. 2, pp. 102-108, May 1989.

[14]   M. Morishita, "Robust controller design for maglev transport vehicles with a guide-selective electromagnetic suspension system," in *Decision and Control*, 1996., Proceedings of the 35th IEEE Conference on, vol. 2, Dec 1996, pp. 1242-1244 vol.2.

[15]   C. H. Kim, H. W. Cho, J. M. Lee, H. S. Han, B. S. Kim, and D. S. Kim, "Levitation control of a hybrid-excited magnetic levitation vehicle," in Control, Automation and Systems (ICCAS), 2011 11th International Conference on, Oct 2011, pp. 1020-1024.

[16]   Y.K. Tzeng and T. C. Wang, "Dynamic analysis of the maglev system using controlled-pm electromagnets and robust zero-power-control strategy," *IEEE Transactions on Magnetics*, vol. 31, no. 6, pp. 4211-4213, Nov 1995.

[17]   F. Sun and K. Oka, "Zero power non-contact suspension system with permanent magnet motion feedback," *Journal of System Design and Dynamics*, vol. 3, no. 4, pp. 627-638, 2009.

[18]   Z. Sun, N. C. Cheung, J. Pan, S. Zhao, and W.-C. Gan, "Design and simulation of a magnetic levitated switched reluctance linear actuator system for high precision application," *IEEE International Symposium on Industrial Electronics*, June 2008, pp. 624-629.

[19]   U. Hasirci, A. Balikci, Z. Zabar, and L. Birenbaum, "A novel magnetic levitation system: Design, implementation, and nonlinear control," *IEEE Transactions on Plasma Science*, vol. 39, no. 1, pp. 492-497, Jan 2011.

[20]   A. Kuijpers, C. Nemlioglu, F. Sahin, A. Verdel, J. C. Compter, and E. A. Lomonova, "Force analysis of linear induction motor for magnetic levitation system," in *Power*

Electronics and Motion Control Conference (EPE/PEMC), 2010 14th International, Sept 2010.

[21]   S. Verma, W. jong Kim, and J. Gu, "Six-axis nanopositioning device with precision magnetic levitation technology," *IEEE/ASME Transactions on Mechatronics*, vol. 9, no. 2, pp. 384-391, June 2004.

[22]   J. Lin, K. Oka, and A. Harada, "Arbitrarily Close Equilibrium Orientations of Magnetically Levitated Platforms," Proceedings of LDIA 17, 2017.

[23]   J. Lin, K. Oka, and A. Harada, "Novel System for Zero-Power, Orientation-Controlled Magnetic Levitation," Proceedings of ISMB 16, 2018.

[24]   C. Zhao, F. Xu, F. Sun, Q. Li, J. Jin, and K. Oka, "Decoupling model establishment and simulation analysis of permanent maglev transmission system," Proceedings of ISFT 7, 2019.

Academic Journal Publications

1. "Zero-Power, Orientation-Controlled Magnetic Levitation by Lateral Displacement of Hybrid-Electromagnets", *International Journal of Applied Electromagnets and Mechanics*. (Pending)

2. "Zero-Power Tip-Tilt Control of Magnetically Levitated Platforms by Lateral Displacement of Permanent Magnets", *International Journal of Applied Electromagnetics and Mechanics*. (Pending)

3. "Proposal for Novel Method of Zero-Power Tip-Tilt Control of Railed Sliders by Flux Path Control of Hybrid Electromagnets". (Collaboration, TBD)

Academic Conference Publications

1. "Arbitrarily Close Equilibrium Orientations of Magnetically Levitated Platforms", LDIA 17, Osaka, 2017.
2. "Novel System for Zero-Power, Orientation-Controlled Magnetic Levitation", ISMB 16, Beijing, 2018.
3. "Bearingless Motor with Non-contact Power Supply", ASCC, 2019.
4. "Design Considerations for a Novel, Zero-Power, Orientation-Controlled, Magnetically Levitated Platforms", ISFT, Thailand, 2019.

Acknowledgements

Firstly, I would like to thank my academic supervisors at the Kochi University of Technology, Dr. Koichi Oka and Dr. Akinori Harada, for allowing me to pursue my academic interests and for providing academic guidance.

Next, I would also like to thank the Kochi University of Technology and the Japan Ministry of Education, Culture, Sports, Science and Technology for their generous financial support.

Of course, I must give recognition to the International Relations Center at the Kochi University of Technology whose assistance in solving cultural and language problems has made living in a foreign country possible.

And finally, I would like to thank my mother and father for instilling in me academic curiosity, and for always pushing me to improve myself.